

1 **Glutathione accelerates the cell cycle and cellular reprogramming in plant** 2 **regeneration**

3 Laura R Lee¹, Bruno Guillotin¹, Ramin Rahni¹, Chanel Hutchison¹, Bénédicte Desvoyes², Crisanto
4 Gutierrez², Kenneth D Birnbaum¹

5 1 New York University, Center for Genomics and Systems Biology, Department of Biology, NY, New York,
6 10003, USA

7 2 Centro de Biología Molecular Severo Ochoa, 28049 Madrid, Spain

8 * Lead contact and Corresponding Author

9 Correspondence: ken.birnbaum@nyu.edu

10 **Summary**

11 The plasticity of plant cells underlies their wide capacity to regenerate, with increasing evidence in plants and
12 animals implicating cell cycle dynamics in cellular reprogramming. To investigate the cell cycle during cellular
13 reprogramming, we developed a comprehensive set of cell cycle phase markers in the Arabidopsis root. Using
14 single-cell RNA-seq profiles and live imaging during regeneration, we found that a subset of cells near an
15 ablation injury dramatically increases division rate by truncating G1. Cells in G1 undergo a transient nuclear
16 peak of glutathione (GSH) prior to coordinated entry into S phase followed by rapid divisions and cellular
17 reprogramming. A symplastic block of the ground tissue impairs regeneration, which is rescued by exogenous
18 GSH. We propose a model in which GSH from the outer tissues is released upon injury licensing an exit from
19 G1 near the wound to induce rapid cell division and reprogramming.

20

21 Introduction

22 Plants have a remarkable capacity to regenerate, where even a single somatic cell can give rise to an entire
23 organism¹. The *Arabidopsis* root apical meristem (RAM) provides a model for regeneration in plants because
24 the organ can regenerate from differentiated cells after removal of the stem niche without exogenous
25 hormones². This process requires the coordination of both cell division and cell identity changes among the
26 cells that will give rise to the new, regenerated tissue. How cell division properties are coordinated with cell fate
27 change in regeneration remains an open question.

28 Prior work in plants has demonstrated links between cell cycle regulation and cell fate specification. In the
29 *Arabidopsis* sepal, giant cells are specified when *MERISTEM LAYER 1 (ML1)* expression exceeds a threshold
30 level during G2/M phase of the cell cycle³. Recent work has shown that high protein levels of the cell fate
31 regulators SHORT ROOT (SHR) and SCARECROW (SCR) at a specific phase of the cell cycle determine the
32 polarity of a formative division in the root⁴. In the stomatal lineage, asymmetric and symmetric cell divisions are
33 mediated by the expression of a series of master regulator basic helix-loop-helix (bHLH) transcription factors
34 that concomitantly regulate cell identity (reviewed in⁵).

35 After specification, cell cycle length frequently changes as cells undergo differentiation. For example, in the
36 root meristem, cell division rates speed up along the maturation gradient as they move away from the stem cell
37 niche during transit amplification⁶, largely due to a shortening of G1 duration as a cell is displaced shootward
38 away from the quiescent center (QC)⁷. Alternatively, in the stomatal lineage, G1 duration increases and cell
39 cycles lengthen as cells commit to terminal differentiation⁸. These observations suggest that even the trends of
40 cell cycle length dynamics during differentiation can differ from tissue to tissue.

41 Different specialized plant cells can also show differences in their core cell cycle machinery. While many core
42 cell cycle regulators are conserved between plants and animals^{9,10}, the expansion of core cell cycle gene
43 families in plants, such as the D type cyclins, has allowed for cellular specialization¹¹. For instance, *CYCLIN D-*
44 *6 (CYCD6)* is specifically expressed downstream of the SHR-SCR module and mediates the switch in division
45 orientation that leads to the formation of a new cell type¹². *CYCLIN D-7 (CYCD7)* expression is restricted to the
46 guard mother cell in the stomatal lineage and regulates a switch from asymmetric to symmetric divisions¹³.
47 This process is also regulated by another specialized cyclin, *CYCLIN D-5 (CYCD5)*¹⁴.

48 These examples suggest that cell type-specific regulation of the cell cycle in plants could be a more general
49 phenomenon, but one challenge facing the field has been studying the cell cycle in a way that maintains the
50 developmental context of cells. Early transcriptional studies of the cell cycle in *Arabidopsis* employed
51 synchronization of cultured cells^{15,16}, which provided valuable insight, but such bulk, *in vitro* analysis could not
52 provide cell type-specific information.

53 Single-cell RNA-seq (scRNA-seq) studies provide an opportunity to analyze cell-type specific properties of the
54 cell cycle, but, outside of G2/M, the ability to map cells to a cell cycle phase is limited. For example, the field
55 lacks a reliable transcriptional marker for the G1 phase of the cell cycle, although CDT1a is a well-supported
56 translational marker^{17,18}. Overall, we have an incomplete view of the extent of cell cycle variation among cells
57 and the transcriptional signatures that distinguish the different ways the cell cycle varies in specific cell types.
58 An extensive set of markers for each cycle phase would add insight into the analysis of cell cycle attributes in
59 the burgeoning collection scRNA-seq studies in plants.

60 In the context of regeneration, cell division is required for complete repair of injured tissues². There is
61 considerable evidence in animals that events during the G1 phase of the cell cycle are critical for cell fate
62 establishment¹⁹⁻²¹, and short G1 phases are a known feature of totipotent animal stem cells²². In plants,
63 division rates can vary dramatically in different contexts. For example, cell divisions in the transit amplifying
64 zone of the root in one study were shown to have a median duration of 21.5 hours⁶. However, other studies
65 showed that cells divide approximately every 7 hours in *Arabidopsis* embryos up until the 16 cell stage²³, and

66 in lateral root primordia cell doubling time has been estimated to be as short as 3.7 hours²⁴. It is not known in
67 plants if rapid divisions facilitate organ formation or cell fate specification in any of these contexts, including
68 regeneration.

69 Both plants and animals can vary division rates by controlling the passage through G1 and G2 checkpoints,
70 which are often regulated by metabolites^{9,25}. For example, it was recently shown that tricarboxylic acid cycle
71 metabolites may regulate root growth and development²⁶. In addition, reactive oxygen species (ROS) have a
72 role in controlling division rates along the root axis²⁷. The tripeptide glutathione (GSH) – the primary antioxidant
73 in the cell²⁸ – is enriched in the nucleus in division-competent cells in both plants and animals with the
74 hypothesized function of protecting newly synthesized DNA from ROS-induced damage (reviewed in²⁹).

75 GSH availability^{30,31} and ROS patterning³² in plants have previously been linked to root growth and cell cycle
76 regulation^{30,32,33}. Prior studies have shown that GSH may be necessary for plant cells to pass the G1 to S
77 transition³⁰ and nuclear ROS levels change cyclically in cell cycle-synchronized root tips³⁴. Finally, evidence
78 from Arabidopsis tissue culture suggests that GSH is transported into the nucleus in a cell cycle-dependent
79 manner with consequences for the redox state of both the nucleus and the cytoplasm³³. Injury, such as RAM
80 excision, results in accumulation of ROS that presumably need to be neutralized by antioxidants³⁵. While both
81 GSH availability and cell cycle regulation are linked to cellular reprogramming following injury, how these
82 factors are coordinated during regeneration, if at all, remains an open question.

83 Here we generate transcriptomic profiles of the cell cycle in the RAM while maintaining developmental context.
84 We synchronize cells in the intact RAM³⁶ followed by scRNA-seq to generate phase-enriched profiles for the
85 G1, S, and G2/M phases of the cell cycle. We corroborate these transcriptional profiles with phase-specific
86 bulk RNA-seq profiles and *in situ* hybridizations to yield a high-confidence set of cell cycle markers. In
87 conjunction with scRNA-seq profiles, we used the markers to analyze the transcriptional composition of each
88 phase of the cell cycle both broadly and among specific cell types. Collective analysis of these datasets
89 reveals 1) many individual cell types have distinct cell cycle dynamics at the transcriptional level and 2) the G1
90 phase of the cell cycle is uniquely tuned to respond to redox stress. During regeneration, we used both single-
91 cell analysis and live imaging to show a dramatic shortening of the G1 phase of the cell cycle in cells near the
92 injury. Furthermore, cells with a short G1 phase reprogram to new cell fates more rapidly than neighboring
93 cells that maintain a longer G1. We demonstrate that GSH mediates both the rapid exit from G1 and fast
94 divisions that preferentially lead to cellular reprogramming. Finally, the results showed that the middle and
95 outer cell types appear to be a major source of GSH in the root that facilitates growth and regeneration.
96 Overall, we show that GSH acts as a signal in regeneration where, upon wounding, GSH enters the nucleus,
97 prompting a rapid exit from G1, a fast cell cycle, and cell-fate reprogramming.

98 Results

99 Phase-enriched scRNA-seq libraries reveal a large set of cell cycle-regulated genes

100 To gain a deeper view of cell cycle dynamics in specific cell types, we sought to characterize cell cycle
101 transcriptomes in intact Arabidopsis roots while maintaining developmental context. To that end, we
102 synchronized cells *in vivo*³⁶ and used scRNA-seq to obtain phase-enriched populations in which cell type-
103 specific information is maintained (Figures 1A and 1B, Figures S1-S2). We normalized the cell type
104 composition for the phase-enriched libraries so that each library contained the same representation of cell
105 types in order to prevent any one cell type from contributing an excess of markers to the final set (Figure S3).
106 We then performed a differential expression analysis as implemented in Seurat³⁷, using the enriched library as
107 the grouping variable and asking for only positive markers that passed a p-value threshold of < 0.01 between
108 the phase-enriched profiles. We ranked the phase markers based on the proportion of cells in which they were
109 expressed in the target versus non-target library to further ensure the selection of cell cycle markers common
110 to all cell types (Table S1). For example, a gene shown to be upregulated in the G1-enriched library was

ranked more highly if it was also expressed in a higher proportion of cells in the same G1-enriched library. This approach identified gold standard cell cycle markers in their appropriate phase (Figure 1C, Table S2).

To corroborate the markers and account for the potential effects of synchronization, we also generated bulk RNA-seq libraries from root cells sorted by ploidy as a proxy for cell cycle phase³⁸. The resulting dataset was analyzed by K-means clustering to reveal the expression patterns of highly variable genes among cell cycle phases. We then analyzed the overlap in cell cycle phase markers between the synchronized single scRNA-seq and bulk RNA-seq profiles (Figure S4). These two approaches overwhelmingly assigned genes to the same phase of the cell cycle (Figure S4).

To corroborate markers for the G1 and S phase, we used the stringent top-50 marker set to assign our synchronized cells to phases in Seurat³⁹ and examined the expression of genes with functional roles in the cell cycle (Figure 1D). With these phase assignments, the origin recognition complex (ORC) family appears to be expressed more highly in G1, while minichromosome maintenance complex (MCM) genes peak in S. This is consistent with the observation that ORCs are required in the pre-replication complex prior to MCMs (reviewed in⁴⁰) and supports that this set of phase markers provides a sensitive discrimination between G1 and S phase.

To validate these markers *in vivo*, we visualized transcripts directly using multicolor *in situ* hybridization (Figure 1E, Figures S3C and S3D). This allowed us to simultaneously visualize a known phase marker in the same plant as a novel probe. Novel markers were selected for *in situ* experiments based on their high expression level and specificity. We observed a novel G2/M marker - AT4G23800 - co-staining with a probe for the well-known G2/M marker CYCB1;1. We observed that both markers overlap in most cells. Additionally, both markers are present in cells with mitotic figures, as visualized by DAPI, further confirming the novel marker is expressed in cells in G2/M phase.

To validate a novel G1 probe, we co-stained a new, putative G1 marker - AT5G21940 - with a well-established S phase marker - AT5G10390 (H3.1)⁴¹, since there are no other documented G1 transcriptional markers. In this case, we tested whether the two markers were anticorrelated with one another and excluded from mitotic figures. As predicted, we found the transcripts of these two genes were both anticorrelated and absent from mitotic figures, with occasional overlap (Figure 1E; Figures S3C and S3D). Thus, the marker set provides a highly sensitive tool for cell cycle analysis in single cell studies and, importantly, a method to distinguish cells in the G1 phase, allowing new analysis of the role of G1 in plants.

The analysis showed that markers for G1 and S phases had expression patterns that were enriched in but not strictly exclusive to their respective phase. For example, S-phase markers, while most highly expressed in that phase, often had low levels of expression in G1 and vice versa. While G2/M is transcriptionally distinct, G1 and S have more continuous expression patterns. However, the full set of markers for each phase, including G1, could robustly assign root cells to a specific phase in scRNA-seq datasets.

The large, high-confidence set of markers allowed us to analyze functional categories in each phase, particularly G1, which has not been deeply characterized. First, as expected, gene ontology (GO) enrichment analysis revealed that cell cycle-related terms were enriched in G2/M using the top 50 marker set and then enriched in G2/M and S phases using the top 200 markers (Figure 1F, Table S3). We found that canonical cell cycle markers are lowly expressed so the most robust markers did not include cyclins (Figure S5). Notably, many markers were enriched in, but not necessarily specific to, any given cell cycle phase, showing that, beyond the distinct transcriptome of G2/M, other phases had less discrete transitions at the transcriptional level.

Interestingly, the top 50 G1 markers were enriched for GO terms related to stress responses (Figure 1F) and closer inspection of a larger marker set showed these terms were specifically related to oxidative stress (Table S3). This enrichment of ontology terms in G1 cells was also present in the G1 ploidy sorted dataset, where cells from all phases were collected from the same pool of cells, ruling out a batch effect (Table S3). This suggests a role for oxidative stress management within G1—an intriguing feature that we pursued below in the

157 analysis of the cell cycle in regeneration. Overall, the dataset now provides a robust tool to analyze the cell
158 cycle in single-cell profiles and identifies new genes with potential roles in specific phases of the cell cycle.

159 **Pseudotime analysis reveals cell cycle variation within and between cell types**

160 We sought to generate a fine-grained analysis of cell type-specific cell cycle patterns in the Arabidopsis root.
161 Using a scRNA-seq profile of all cells in the root meristem⁴², cells were aligned in a pseudotime trajectory with
162 Monocle3⁴³ using only the top 150 cell cycle markers and visualizing them in Uniform Manifold Approximation
163 and Projection (UMAP⁴⁴, Figure 2A). The trajectories are anchored in G2/M and proceed to G1 where they split
164 into three separate branches that each continue to S phase. To map cell identities onto cell cycle-annotated
165 single cells, we used cell-identity markers identified in an independent analysis⁴². Despite filtering out cell type-
166 specific markers in the original ordering, different cell types still favored—but were not restricted to—distinct
167 regions of the UMAP space (Figure 2B, Figure S6). This indicated that, using only a core set of shared cell
168 cycle markers, cells still clustered by their *in vivo* identity, suggesting the separate branches for one cell cycle
169 phase represented cell type-specific cell cycles.

170 The most apparent trend was a difference in G1 to S branches between inner and outer cell types. Xylem and
171 phloem occupied successive layers of a left branch, with endodermis and cortex on an outermost layer of the
172 branch (Figure 2B). Epidermal cell types occupied a distinct second branch, and a third branch contained the
173 slow cycling cells around the quiescent center (QC), the core of the stem cell niche (Figure 2B). This distinct
174 stem cell behavior is in accordance with the well-documented slower rate of division of these cells compared to
175 the more proximally located (shootward) transit amplifying cells^{6,7,45}. Indeed, the epidermal G1 branch is
176 enriched for genes related to translation, while the stele-endodermis-cortex G1 branch is characterized by
177 gene expression related to cell wall synthesis (Figure 2C, Table S4). This suggests that the specialized
178 functions of specific cell types are at least partially regulated within the cell cycle as they mature in the
179 meristem. This is consistent with the hypothesis that plant cells have multiple G1 modes⁴⁶.

180 In addition, we observe two subpopulations of cells in G2/M, separated into an upper and lower branch (Figure
181 2A). While many genes were commonly expressed across G2/M cells, we found unique functional enrichments
182 between these branches. The upper branch expressed genes that regulate the G2/M transition, while the lower
183 branch expressed cytokinesis regulators (Figure 2D). These two branches reveal a set of *in vivo* G2/M
184 processes shared by all cell types.

185 Nonetheless, we observed cell type-specific biases within the different regions of the G2/M branch, potentially
186 indicating differences in the amount of time cells spent in a given sub-phase of G2/M (phase dwelling). To test
187 this hypothesis *in vivo*, we generated long-term time-lapse light sheet microscopy movies of roots expressing
188 the three-color cell cycle translational reporter, PlaCCI, which marks G1 (CDT1a, cyan), S (HTR13, red), and
189 Late G2 through M phase (CYCB1;1, yellow¹⁸). We measured G2/M duration in epidermal, cortical, stele, and
190 lateral root cap cells (Figure 2E, 2F, movies S1). From one such time lapse, epidermal and cortical cells
191 remained in G2/M twice as long as stele and lateral root cap cells. But there was also significant variation in
192 G2/M duration within cell types. For example, the length of epidermal G2/M ranged from 01:00 to 10:10
193 (hh:mm) and the range was 00:10 to 01:50 in the stele (Figure 2F). Thus, live imaging corroborates the cell
194 type-specific phase-dwelling variations detected by the cell cycle mapping of scRNA-seq profiles. Overall,
195 these observations reveal the extent to which the cell cycle is tailored to cell identity and developmental stage.

196 **Tissue-wide coordinated G1 exit and rapid G1 is linked to regeneration efficiency**

197 Many questions in plant and animal regeneration concern how cell cycle regulation mediates cellular
198 reprogramming. For example, we have observed that cell cycle speed increases during RAM regeneration⁴⁷,
199 but it remains unclear whether this is due to a uniform increase in cell cycle speed across phases or whether
200 certain phases are truncated to achieve fast divisions. Thus, we applied the cell cycle marker analysis to

single-cell analysis of regenerating cells in the excised root tip over a time course of 4 to 36 hours post-injury to analyze their fine-grained cell cycle dynamics. We focused on the relatively small set of cells actively contributing to regeneration, as previously annotated⁴², aligning regenerating single-cell profiles in cell cycle pseudotime, similar to above. The analysis showed that regenerating cells disproportionately accumulate at the G1 to S transition and are largely absent from G1 phase (Figure 3A).

This result suggests that G1 is dramatically shortened relative to the other phases of the cell cycle during early regeneration, raising the possibility that cells undergoing reprogramming truncate G1. To measure G1 duration together with fate re-specification, we used time-lapse light sheet imaging on live regenerating roots, quantifying G1 phase duration concurrently with cell fate changes. In the root tip regeneration system, the meristem is excised, completely removing the QC and columella cells, which are then respecified within a day from vascular and other cells left in the cut stump². To enable rapid imaging after regeneration, we generated a similar root-tip excision using a two-photon ablation system in which the root meristem is essentially isolated by a plane of dead cells causing regeneration of QC and columella shootward, as in root tip excision (see below). We used the *PlacCI*¹⁸ marker to track cell cycle phase and the QC-columella marker *WIP4* to track cellular reprogramming⁴⁸. Return of *WIP4* expression shootward of the ablation site marks cells that are in the process of adopting QC and columella fates in the newly formed meristem – a key step of RAM regeneration. By monitoring this region, we could track the full history of cell cycle phases, their duration, and reprogramming state.

We observed that cells in the regeneration zone coordinately exited G1 approximately 6 hours post-injury, within 1 to 2 hours of one another, depending on biological replicate, and prior to new *WIP4* expression (Figures 3B and 3C, Movies S2, S3). This results in a significant decrease in the number of G1 cells between 6 to 8 hours after injury (p-value = 0.008047), while the number of S cells does not change (Chi Square test; p-value = 0.3118), consistent with the dramatic depletion of G1 detected in the scRNA-seq analysis of regenerating cells.

Between 8 to 12 hours post-injury, cells proceeded through G1 at an accelerated rate (Figure 3D, 3E). To quantify G1 length, we measured the elapsed time between when *CDT1a* became visible after mitosis (early G1) to when *CDT1a* was degraded, indicating S-phase entry. Some of the observed G1 events did not end during the time lapse in both the control (76 percent) and the ablation (38 percent) movies. In these cases, we measured G1 duration in three ways: 1) as the time between when *CDT1a* became visible and the final frame of the time lapse, 2) as equal to the observed G1 duration time for this region of the root, which is estimated to be longer than 20 hours⁷, and 3) as the fraction of total movie duration (Table S5). By all these metrics, the difference in G1 duration is statistically significant (Mann-Whitney test, p-value = 1.614e-08, p-value = 2.04e-05, or p-value = 3.221e-09). Thus, the specific, highly localized set of cells that will reprogram to generate the new root tip undergo much more rapid G1 than their neighbors.

To test the association between rapid G1 and reprogramming, we identified cells that eventually expressed the *WIP4* marker (indicating cellular reprogramming, Figure 3F) and analyzed their cell cycle dynamics retrospectively in the time-lapse movies. We compared the timing of re-specification in cells with short G1 vs. neighboring cells that displayed longer G1s (Figure 3G). We categorized cells based on short, medium, and long G1 and S duration. While cells gained *WIP4* expression at a similar rate regardless of S phase duration, cells with short G1 gained higher *WIP4* expression levels than nearby cells with long G1 (Figure 3G). There was no relationship between *WIP4* expression and G1 duration in unablated roots (Figure S7). Thus, a specific group of cells in the regenerating stump that undergo fast G1 reprogram more rapidly than slower G1 neighbors.

To determine whether the relationship between G1 length and re-specification holds for other markers that are expressed later during regeneration, we looked at a late-stage marker for columella, *PET111*. In this case, we exploited variability in *PET111* return time and G1 duration between roots to explore whether these two variables were correlated. In this analysis, G1 duration was broadly predictive of *PET111* re-appearance

(Figure 3H). For example, a root in which the median G1 duration was 1.5 hours began to express PET111 in the regeneration domain at 20 hours post-injury. A second root in which median G1 duration was 2.7 hours began to express PET111 at 28 hours post-injury. Thus, we conclude that rapid G1 phases in plant root regeneration facilitate the complete, *de novo* reprogramming of excised cell fates.

GSH is enriched in G1 nuclei at steady state and immediately following tissue damage

Having implicated G1 duration in control of regeneration efficiency, we next sought to establish a mechanistic link between injury and cell cycle regulation. The finding above showing “response to wounding” and “response to oxygen-containing compound” terms enriched in G1 was intriguing because ROS has potential links to both the cell cycle and wounding (Figure 1F). In particular, GSH is the primary antioxidant in the cell, and GSH levels in the nucleus have been found to vary over the course of the cell cycle in both plants and animals³². In Arabidopsis, GSH has been demonstrated to be necessary for the G1 to S transition in root formation³⁰. In addition, ROS generation is a hallmark of tissue damage³⁵, with variants in genes controlling thioredoxin-mediated ROS associated with natural variation in regeneration capacity in Arabidopsis⁴⁹. Thus, we reasoned that G1 cells could be primed to respond to ROS signals generated by tissue damage.

To explore this connection, we performed live imaging with the ROS indicator H2DCFDA and the GSH dyes blue CMAC and CMFDA during stereotypical root growth and regeneration (Figures S8 and S9). We first confirmed that these dyes had no effect on meristem size and regeneration efficiency (Figure 4A). We used time-lapse confocal imaging and the ablation described above to observe GSH localization within the first 30 minutes of tissue damage. We distinguished cells in G1 vs S phase using the PlaCCI marker (noting that the S-phase mCherry marker is also expressed in early G2 phase¹⁸). We found that, in control roots, blue CMAC signal was higher in G1-phase nuclei than in S phase nuclei (Figure 4B), building on prior evidence that suggested nuclear GSH controls the G1 to S transition^{30,33}. In regeneration, we observed a pulse of nuclear GSH immediately after ablation just above the injury site (Figures 4C-4E, Movie S4). In addition, in the root cutting injury, at the 2- and 4-hours post cut (HPC) time points, nuclei that showed the highest CMAC signal shootward of the cut site were in the same region in which cells undergo rapid G1 phases (Figure S10). Overall, the results suggested that the earliest cells to reprogram first undergo a local burst of GSH import into the nucleus then exhibit a coordinated G1 exit followed by a rapid G1 phase.

GSH depletion inhibits regeneration efficiency

To explore the functional role of GSH in regeneration, we depleted GSH during regeneration using the GSH synthesis inhibitor, L-Buthionine-sulfoximine (BSO), following similar treatments in Arabidopsis³¹. We first depleted GSH in roots by germinating seedlings on plates supplemented with 1 mM mM BSO (Figures 5A and 5B), as used previously³¹. We performed this experiment on seedlings expressing PlaCCI and the WIP4 transcriptional reporter to simultaneously track cell division and QC reestablishment, while also using blue CMAC staining to visualize GSH.

The control seedlings regenerated a new QC shootward of the ablation over the course of 72 hours (Figure 5B). Seedlings germinated on 1mM BSO were depleted for blue CMAC signal (Figure 5A), and they showed weak WIP4 expression shootward of the ablation through 72 post-injury. In addition, these roots failed to form an expression pattern indicative of new QC establishment (Figure 5B). However, as previously shown³¹, we observed that most seedlings treated in this manner had short roots before the ablation, raising the possibility that meristem defects before ablation impaired regeneration. To address this issue, roots were germinated on a lower concentration of BSO (0.5mM) on which they displayed normal morphology³¹. Although ablated roots grown on this lower BSO concentration eventually regenerated, they showed a lower amount of WIP4 expression in the regeneration zone at 24 hours post-injury (Figures 5C and 5D). Thus, depletion of GSH to a

291 level that does not affect stereotypical root growth still impairs the re-specification of the columella and QC
292 marker.

293 Columella cells are necessary for the root to sense gravity, which requires ballast-like organelles called
294 amyloplasts that settle along the gravity vector. Thus, amyloplasts are a functional marker for columella re-
295 specification. To quantitatively assess the effect of GSH depletion on regeneration efficiency, we monitored the
296 number of cells containing amyloplasts in excised root tips with modified Pseudo Schiff-Propidium Iodide
297 (mPS-PI) staining⁵⁰ at 18 hours post-injury in four conditions: mock, 0.5 mM BSO, 0.5 mM GSH, and 0.5 mM
298 BSO + 0.5 mM GSH combined. We found that treatment with BSO significantly decreased the number of cells
299 with *de novo* amyloplasts at 18 hours and that co-treatment with GSH rescued regeneration to the level of
300 untreated roots (Figures 5E and 5F), consistent with regeneration defects caused by diminished levels of GSH
301 post-injury.

302 We next directly tested whether BSO treatment perturbs G1 dynamics during regeneration by performing long-
303 term time-lapse imaging in the PlaCCI line with roots germinated on 0.5 mM BSO. We found that following
304 injury, G1 cells in BSO-treated roots failed to undergo the coordinated exit that we observed in untreated roots
305 (Figure 6A). We formalized this observation by performing a survival analysis, recording how long it took cells
306 in G1 at the beginning of the time lapse to enter S phase (Figure 6B). We found that the time cells remained in
307 G1 was significantly prolonged in BSO-treated roots (log rank test; p value < 2e-16). In addition, the
308 presumptive new columella cells failed to develop their characteristic columnar cell morphology within 24
309 hours, indicating a defect in regeneration (Figure 6C). Interestingly, BSO appeared to have a greater effect on
310 cells away from the immediate injury site. For example, in BSO-treated roots, most cells above the injury failed
311 to exit G1 in a coordinated manner, while the first two or so layers of cells near the cut site still showed the
312 coordinated exit despite BSO treatment (Figure 6D). This is consistent with a gradient of GSH that is highest in
313 cells immediately adjacent to the wound site dissipating in more proximal cells, where BSO was presumably
314 more competent to disrupt GSH signaling. Overall, the effects of the BSO treatment on cellular morphology,
315 WIP4 expression levels (Figure 5C, 5D), amyloplast formation (Figures 5E and 5F), and G1 dynamics lead to
316 the conclusion that GSH depletion slows regeneration at least in part through modifying G1 exit and duration.

317 **Ground tissue is a major source of glutathione in growth and regeneration**

318 In our staining for GSH in unablated roots, we observed a striking pattern in which blue CMAC was highly
319 localized to the cap, epidermis, and ground tissue (cortex and endodermis), while the stele stained much more
320 weakly (Figure 4A, leftmost panel). The pattern did not appear to be an artifact of limited cell penetration, as
321 the two GSH dyes Blue CMAC and CMFDA have similar staining patterns, while the ROS indicator H2DCFDA,
322 which has a similar chemical structure to CMFDA⁵¹, stains all files relatively evenly (Figure S8A). In particular,
323 with both blue CMAC and CMFDA, we observed highly concentrated staining in the endodermis and cortex
324 (Figure S8A). The localization pattern was consistent with independent data we gathered from scRNA-seq
325 studies that showed GSH biosynthesis genes are also highly expressed in the ground tissue (Figure S8B). This
326 led us to hypothesize that ground tissue could be a source of GSH for root growth and rapid dissemination
327 upon injury.

328 Metabolites and other small molecules can travel rapidly between plant cells through symplastic connections
329 that form tunnels between adjacent cell walls called plasmodesmata⁵². To ask whether ground tissue could
330 serve as a source of GSH for other files to enable homeostatic growth and regeneration, we employed a
331 callose synthase induction system that blocks symplastic transport out of endodermis and the cortex⁵³ and
332 then assayed for growth (Figure 7A) and regeneration efficiency (Figure 7B). Exogenous GSH is known to
333 enhance growth rates in Arabidopsis roots, so we controlled for the nonspecific effects on growth by
334 comparison to high sucrose (1% versus the standard 0.5%), which also enhances root growth. Accordingly,
335 both sucrose and GSH both increased growth rates in control roots. However, only GSH-treated roots partially
336 rescued the growth of the ground-tissue blocked roots (Figure 7A). Furthermore, after injury and symplastic

337 block of the ground tissue, GSH, but not sucrose, rescued regeneration efficiency (Figure 7B). We conclude
338 that ground tissue is a source of GSH for normal growth and tissue regeneration, licensing rapid exit from G1,
339 an abbreviated cell cycle, and rapid cellular reprogramming.

340 Discussion

341 There are clear connections between cell division and cell fate decisions across the kingdoms of life. In the
342 context of root tip regeneration, cell division is known to be necessary to enable complete root tip repair after
343 excision². Here, we leveraged the ability to induce cellular reprogramming and closely monitor cells with both
344 time-lapse microscopy and transcriptomics in root tip regeneration to demonstrate that the rate of cell division,
345 mediated by dramatic alteration of G1 phase, has a direct influence on cellular reprogramming. In our findings,
346 glutathione (GSH) mediates fast divisions via truncated G1 phase in a small number of cells that will go on to
347 reprogram their fate first. Furthermore, we found that the ground tissue is an important source of glutathione for
348 stereotypical growth and regeneration. Given the findings, we posit a model in which GSH produced in the
349 ground tissue rapidly disseminates to nearby tissues after injury. The GSH stores are preferentially imported
350 into the nucleus of a subset of cells near the injury site where they instigate coordinated exit from G1 and
351 accelerated cell divisions that permit rapid cellular reprogramming.

352 The root has distinct inner, outer and promeristem cell cycles

353 Using bulk and scRNA-seq, we defined a novel list of cell cycle phase markers, including a large set of G1
354 markers, which now provide a resource for the plant community, particularly for analysis of the cell cycle in
355 scRNA-seq studies. By clustering cells based on cell cycle-regulated genes, we detected multiple paths
356 through G1 indicating that distinct G1 states exist in Arabidopsis roots (Figure 2A). We took several steps to
357 ensure that cell type-specific markers were filtered out of the cell cycle phase markers, even if they appeared
358 to be phase-specific. Nonetheless, mapping cell identities onto the cell cycle trajectory revealed that different
359 cell types appear to prefer unique paths through the cell cycle (Figure 2B, Figure S6). For example, in one G1
360 phase pseudotime path, xylem and phloem cells appeared to occupy distinctly different layers of a left branch,
361 while trichoblasts largely occupied a central branch. Genes expressed in the xylem-phloem branch are
362 enriched for GO terms relating to auxin response and developmental processes (Figure S6). The genes that
363 were selected as cell cycle phase markers are widely expressed across cell types, so the groupings by cell
364 identity must reflect how these commonly expressed genes are specifically regulated in a given cell type. It is
365 feasible that common facets of plant cell biology—such as construction of a cell wall, which also varies among
366 cell types⁵⁴—are linked to changes in the cell cycle⁵⁵ to accommodate differences among cell types.

367 The most robust cell-cycle markers we identified represent non-canonical cell cycle genes (Figure 2E). This is
368 evidenced by the fact that, while core cell cycle regulators behave well in our datasets (Figure 1C, 1D, Figure
369 S5), few genes we identified as being most highly cell cycle-regulated are among the genes considered to be
370 core cell-cycle regulators (Table S1). It has been argued previously that different occurrences of cellular
371 quiescence in plants – meristematic quiescence, dormancy, and terminal differentiation – are regulated
372 distinctly and by non-canonical cell cycle genes⁴⁶. Our results show that multiple subpopulations of G1 cells
373 exist and that they are characterized by the expression of distinct transcriptional modules. One subpopulation
374 is characterized by the expression of genes relating to cell wall synthesis, while the other is characterized by
375 genes regulating translation, both of which are functions that have been tied to the G1 phase in plants^{55,56}.
376 Another recent report has shown that the longitudinal axis of the root is largely due to variation in G1 length⁷.
377 Our results support a general model in which the cell cycle is finely tuned to both the maturation stage, as is
378 well documented, but also to cell identity.

379 In addition to the ability to detect multiple G1 phase cell populations, we also find evidence for two G2/M
380 populations, which express genes related to checkpoint regulation or cytokinesis respectively. In parallel, our *in vivo*
381 data shows that distinct cell types spend different amounts of time in G2/M in the RAM. This indicates our

cell cycle marker set can be used to detect cell cycle sub-phases in Arabidopsis scRNA-seq data and enable further dissection on cell cycle regulation in existing and future plant scRNA-seq datasets.

Reprogramming plant cells divide rapidly by truncating G1

In metazoans, evidence links rapid G1 phases with competence to reprogram^{57,58}. For example, embryonic stem- and induced-pluripotent cells are characterized by rapid cell cycles with short G1 phases⁵⁷. In plants, while division times in the indeterminately growing meristems are about 20 hours⁶, cell division rates during embryogenesis, lateral root formation, and root regeneration – all instances of novel root formation rather than homeostatic growth – show a dramatic acceleration to 3 to 7 hours^{23,24,47}. Here, we show that the fast divisions in regeneration are largely due to a highly truncated G1, consistent with data from efficiently reprogramming murine hematopoietic progenitor cells⁵⁸—another context in which dramatic changes in the cell cycle are mediated by alterations in G1.

G1 has been shown in metazoans to be a key point in which cells are receptive to signals that promote specialized cell fate and differentiation^{59–61}. Thus, it has been posited that rapid G1s allow cells to remain pluripotent by avoiding differentiation signals^{59–61}. In our scRNA-seq profiles, we did not detect any enrichment of known cell identity markers in a given phase of the cell cycle. Thus, we have no evidence that short G1s could bypass differentiation signals, although we cannot rule out that cell fate markers are induced synchronously but transcribed at different rates or regulated at another level as has been shown for some specific contexts in plants^{3,4}. Nonetheless, our experiments clearly associate rapid G1 phases and coordinated G1 exit with the competence to reprogram cell fate across cell types. Importantly, neighboring cells that did not undergo rapid G1 phases could still reprogram, and, while treatments that perturbed G1 coordination showed slower regeneration dynamics, even injured roots exposed to such treatment eventually regenerated. Thus, rapid and coordinated G1s are not absolutely necessary for cellular reprogramming. It is not clear if G1 dynamics during regeneration have a direct role in avoidance of differentiation signals, or, if rapid G1s might simply allow a faster entry into S phase. While mechanisms have been identified to link maintenance of histone modifications to DNA replication in plants^{62,63}, there is inherent potential for remodeling the chromatin landscape during DNA synthesis through new histone deposition⁶⁴.

Another possibility is that regulation of G1 may simply be the best option to control overall speed of the cell cycle. Several studies have shown that wound responses in plants reflect a bet-hedging strategy that balances defense responses with regenerative growth^{65–68}. A similar bet-hedging strategy may have evolved to control cell cycle speed. It has been observed that plant stem cells divide infrequently to limit accumulation of replication-induced mutations⁶⁹. However, wounding creates stresses, such as increased susceptibility of plants to pathogens⁷⁰, that require a rapid response. An ability to trigger fast divisions in otherwise slow-dividing cells may have evolved to limit risks of pathogen exposure following wounding. The ability to pass through G1 quickly and enable rapid divisions may simply represent an adaptation that permits more rapid wound healing and leaves the plant less vulnerable to pathogen attack. Of course, rapid G1s could have multiple roles in regeneration due to a combination of factors.

G1 cells are primed to perceive tissue damage via GSH nuclear influx

Prior studies have shown evidence that GSH is necessary for the G1 to S transition³⁰, while *in vitro* experiments showed that GSH is imported into the nucleus during G1³³. We showed here that GSH is enriched in G1 nuclei during normal development (Figure 4B) and is transiently increased in G1 nuclei following tissue damage (Figure 4D, 4E, Figure S10). We further present evidence that this transient influx regulates G1 exit during regeneration *in vivo* (Figure 6). Our live-imaging experiments showed that GSH is rapidly nuclear localized in G1 cells, some of which will go on to become the new stem cell niche. This implies that G1 nuclei are inherently more able to take up GSH than those of cells in other phases. Interestingly, when BSO

426 treatment is used to deplete GSH, we find that only the cells closest to the wound site maintain coordinated G1
427 exit (Figure 6D). This appears to reflect higher levels of GSH closer to the wound, which is feasibly a source of
428 GSH following injury.

429 Together the evidence leads to a model that could potentially link damage-sensing with cell cycle regulation.
430 G1 nuclei are primed to perceive damage to neighboring cells via GSH nuclear permeability. In this model,
431 GSH released from lysed cells, either directly or by modulating overall nuclear ROS, serves as a damage-
432 sensing signal that allows plant cells to respond to injury by increasing cell cycle speed in close proximity to the
433 wound site.

434 How G1 nuclei maintain higher GSH permeability than nuclei in other phases of the cell cycle remains an open
435 question. While there is good evidence that the OPT family of genes control intercellular GSH transport in
436 plants (reviewed in⁷¹) and the CLT family of genes control GSH transport between the cytoplasm and
437 plastids⁷², the mechanism through which GSH is preferentially imported into G1 nuclei in plants is not known⁷³.
438 In animals, Bcl-2 has been implicated in the GSH nuclear import⁷⁴. However, plants have no apparent
439 orthologs to Bcl-2. Looking forward, identification of the mechanism responsible for mediating transport of GSH
440 into G1 nuclei will represent a key link between wound signaling and cell cycle regulation in plants.

441 **Regeneration competence is associated with high levels of GSH across kingdoms**

442 Several lines of evidence in our study pointed to a special role for the endodermis and outer tissues in
443 controlling GSH availability. First, regeneration was impaired when we inhibited the movement of GSH out of
444 the endodermis and cortex (ground tissue) by blocking symplastic connections (Figure 7). Even though both
445 GSH and sucrose enhanced plant growth in general, GSH--but not sucrose--could rescue inhibition of
446 regeneration caused by endodermis and cortex symplastic isolation. In addition, our staining experiments
447 showed GSH is enriched in the endodermis and cortex (Figure S8)--the same tissue where our independent
448 scRNA-seq experiments showed the enzyme for the rate limiting step in GSH synthesis highly enriched⁴².

449 There is ample evidence that the ground tissue has a specific role in controlling root growth. First, mutants that
450 affect ground-tissue identity, such as *scr* and *shr*, lead to severely stunted roots^{75,76}. In addition, it was shown
451 that rescuing SCR function only in the endodermal tissue (leaving out its quiescent center domain) partially
452 rescues *scr* mutants' growth defect⁷⁷. Some of the endodermal control appears to be mediated by hormone
453 signaling, particularly during stress (reviewed in⁷⁸). Our data suggests that another way that the endodermis
454 controls growth is as a source of GSH to promote G1 exit and advance the cell cycle. In addition, we implicate
455 a unique role for the endodermis in regeneration where it appears to provide a rapid flux of GSH through
456 plasmodesmatal connections (Figure 7).

457 The association between GSH levels and the competence to regenerate is another trait shared across
458 kingdoms. In animals, the liver also has the highest capacity to regenerate among solid organs⁷⁹. The liver is
459 also the organ with the highest GSH levels⁸⁰, and, as in root regeneration, liver regeneration is also inhibited by
460 perturbation of GSH levels via BSO treatment⁸¹. Thus, the metabolic environment and core signaling properties
461 of GSH may establish some of the competence of regenerative tissue.

462 The regulation of G1 by GSH import and the involvement of fast divisions in pluripotency are remarkably
463 similar facets of regeneration in plants and animals, even if the specific mechanisms have diverged. As efforts
464 are underway in both kingdoms to improve regeneration, the mechanisms that control rapid G1 are promising
465 tools to control the process. Our study points to a remarkably conserved role for GSH and its role in G1
466 truncation and highlights the role of the metabolic environment in regeneration.

467 **Limitations of the study**

468 Several corroborating lines of evidence supported our localization of GSH in the root and we used multiple
469 methods to validate cell cycle reporters. Nonetheless, first, we point out that this work relies on dyes to
470 visualize GSH in vivo rather than direct visualization. While direct visualization of GSH is possible via mass
471 spectroscopy imaging, the spatial resolution of this technique is not yet fine enough to achieve cell type-
472 specific resolution in the Arabidopsis root, where many cells are smaller than 10 microns in the x and y
473 dimensions. Further, direct GSH biosensors are not currently available for plants. It will be important to
474 examine GSH localization directly via live imaging when the requisite technology becomes available. The
475 second limitation relates to our isolation of cells by phase using FACS. In the ideal case, we would have used
476 the cell cycle readout of PlaCCI using FACS to define cell cycle phase to obtain bulk protoplast populations
477 using the markers from each phase alone from the same batch of roots. However, we found that the CDT1a
478 and CYCB1;1 fluorescent fusion proteins that mark G1 and G2/M phases in the PlaCCI reporter rapidly
479 diminished in protoplasts. The PlaCCI reporter enabled significant advances in the ability to study the cell cycle
480 in plants in vivo. In addition, the work shows the role of fast divisions in rapid cellular reprogramming. However,
481 it does not address how rapid vs. slower reprogramming could provide an advantage to the plant. Further work
482 could focus on the ecological or physiological advantages or tradeoffs of rapid cellular reprogramming in
483 regeneration.

484 **Acknowledgements**

485 This work was supported by a Postdoctoral Research Fellowship in Biology from the National Science
486 Foundation (2109634) to L.L. and the National Institutes of Health (R35GM136362) to K.D.B. We would like to
487 thank Dominique Bergmann, Michael Raissig, Ximena Anleu-Gil, Martin Bringmann, and Joseph Cammarata
488 for helpful discussions.

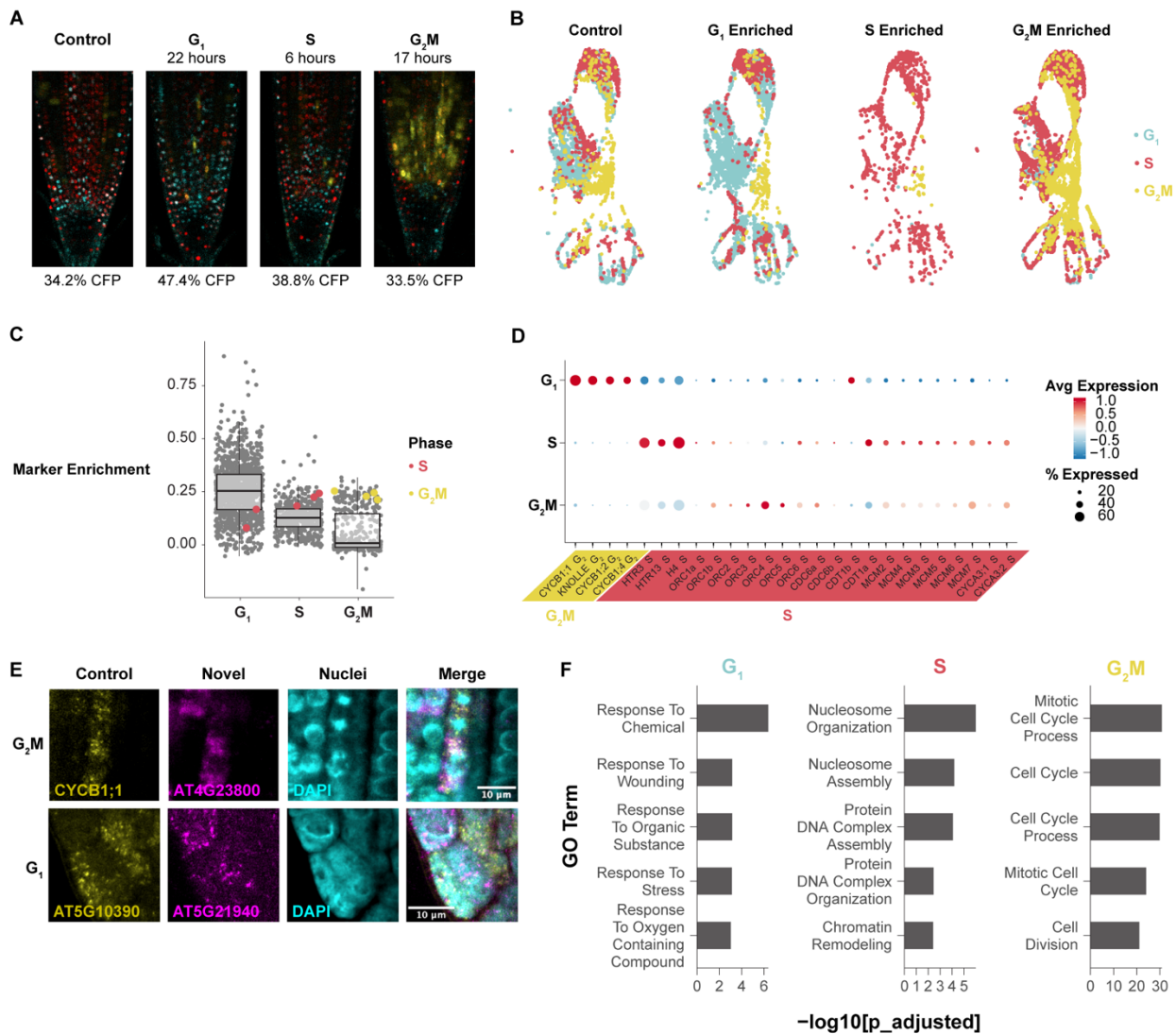
489 **Author contributions**

490 L. R. L.: Conceptualization, Methodology, Validation, Formal analysis, Investigation, Writing - Original Draft,
491 Writing - Review & Editing, Visualization. B. G.: Resources, Data Curation, Writing - Review & Editing. R. R.:
492 Investigation, Writing - Review & Editing, Visualization. C. H.: Investigation. B. D.: Resources, Writing - Review
493 & Editing. C. G.: Resources, Writing - Review & Editing. K. D. B: Conceptualization, Methodology, Writing -
494 Original Draft, Writing - Review & Editing, Supervision, Funding acquisition.

495 **Declaration of Interests**

496 The authors declare no competing interests.

497 **Main Figure Titles and Legends**



498

499

500

501

502

503

504

505

506

507

508

509

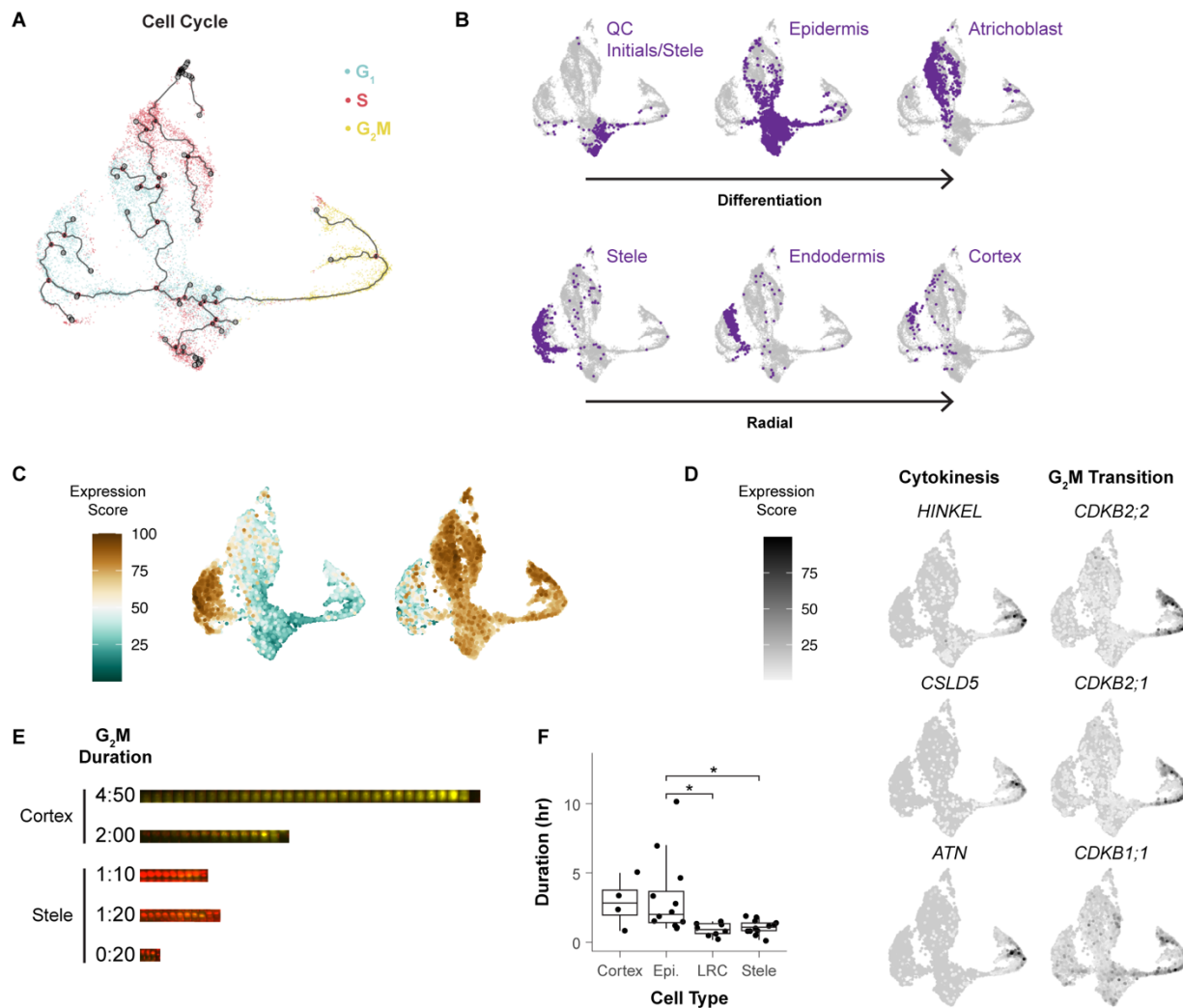
510

511

512

513

Figure 1: Single-cell phase synchronized cells yield robust transcriptional markers for each phase of the cell cycle. (A) Representative images of phase enrichments achieved with HU synchronization using seedlings expressing the PlaCCI reporter. G₁ cells are shown in cyan, S cells are shown in red, and G₂/M cells are shown in yellow. (B) An unsynchronized control and three single cell profiles collected at specific times after synchronization integrated in UMAP with cells color coded by phase determination. Cells from each time point were separated after integration. (C) Genes (each dot) categorized as differentially expressed in specific phase-synchronized libraries. The y axis represents the difference in the percentage of cells in which the gene is expressed in target versus non-target libraries. The highlighted genes are gold standard markers of phase-specific expression, showing high expression in many cells in the appropriate phase-synchronized library (x axis categories). (D) A dot plot showing expression of gold standard cell-cycle phase markers, showing known G₂/M-phase markers (CYCBs) followed by known S-phase markers. (E) *In situ* hybridization of novel G₁ and G₂/M probes. Known markers are shown in yellow and new markers in magenta. The new G₂/M marker is hybridized with a known G₂/M marker, showing overlap. The new G₁ marker is hybridized with a known S marker, showing spatial anticorrelation. (F) The top five most statistically significantly enriched GO terms in the top 50 phase marker set for each phase. See also Figures S1-S5 and Tables S1-S3.



514

515

516

517

518

519

520

521

522

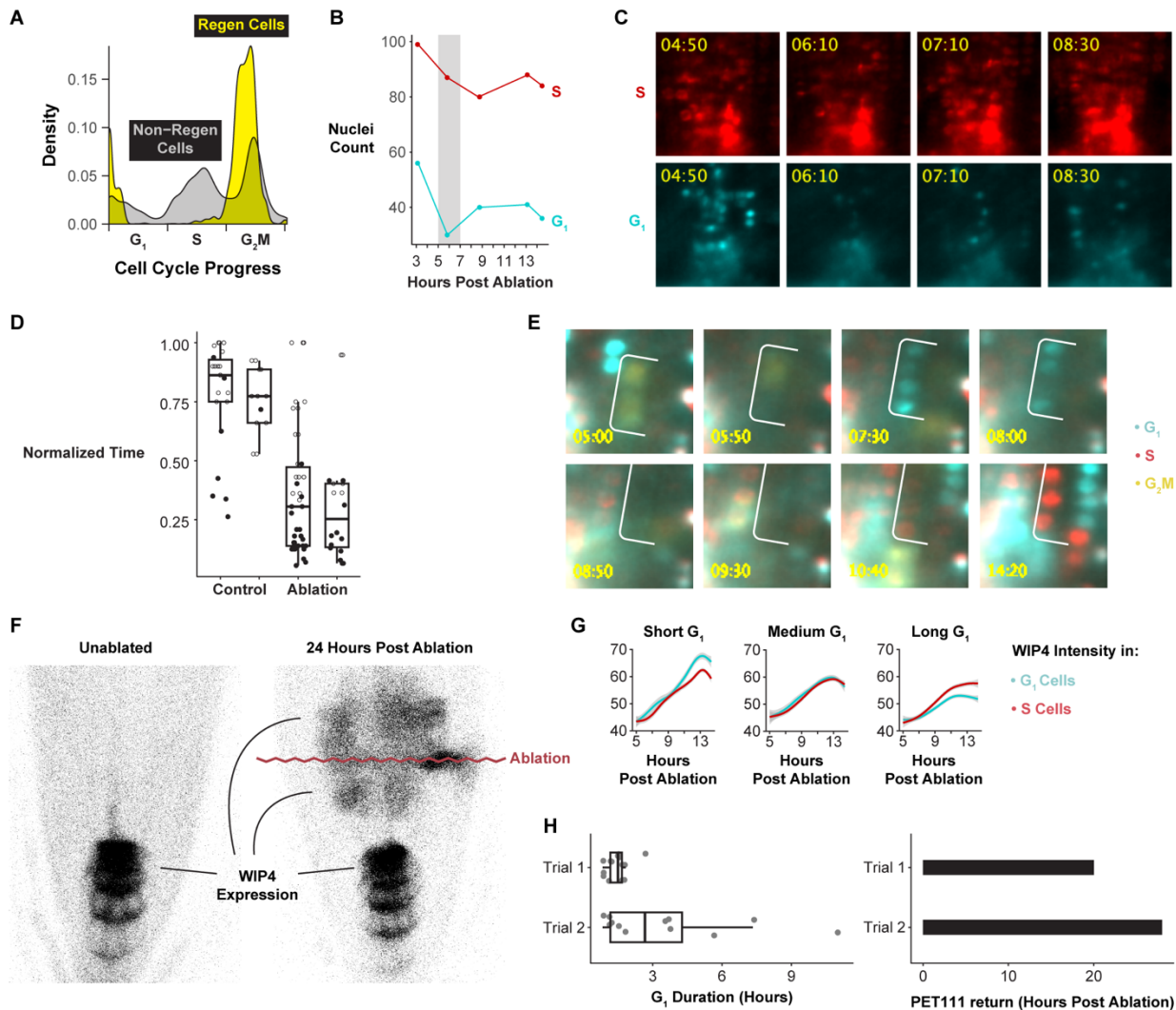
523

524

525

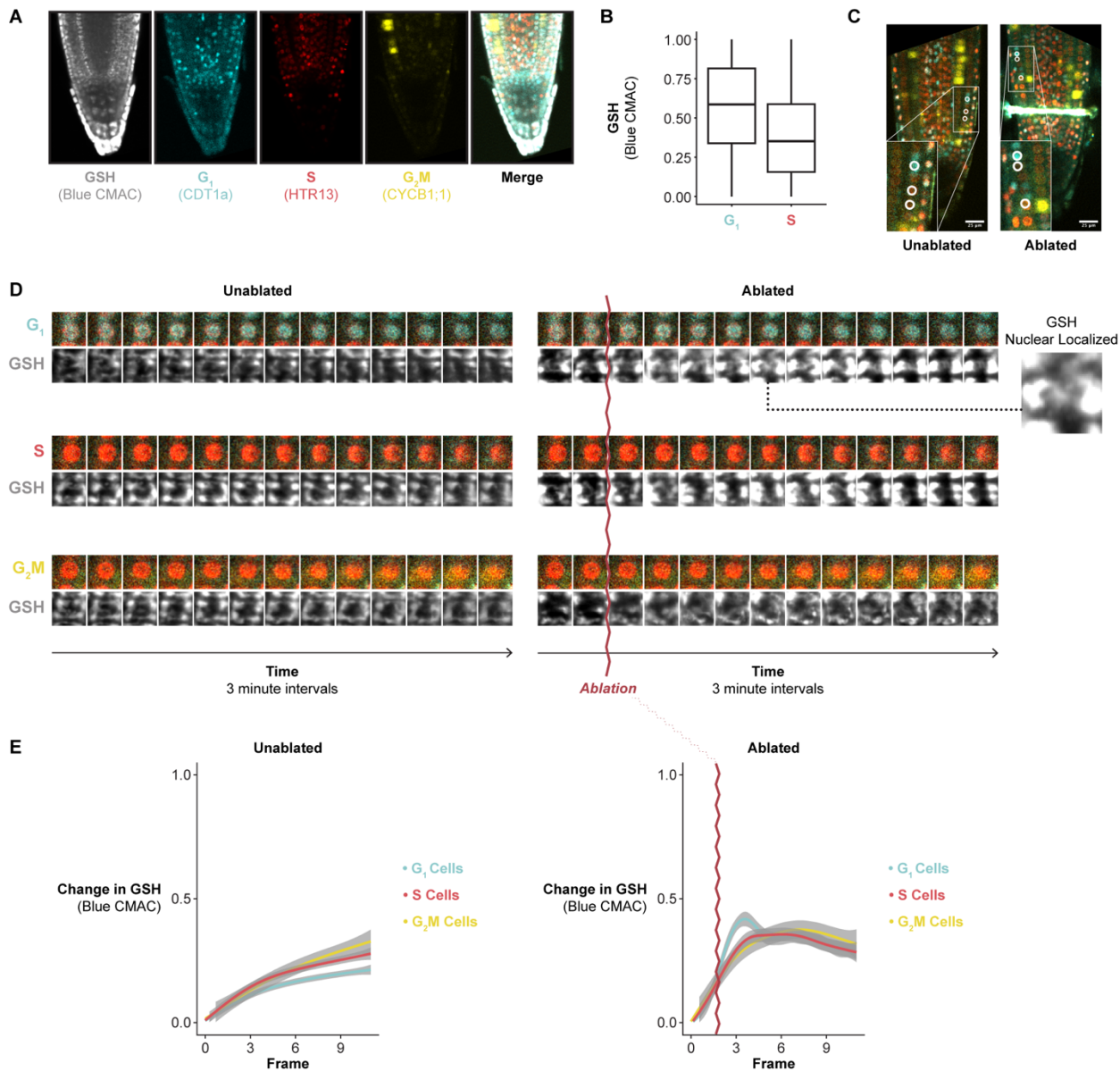
526

Figure 2: Different cell types follow different trajectories through the cell cycle. (A) Pseudotime map of cells clustered using only cell cycle markers and colored by phase assigned in Seurat. (B) In the same UMAP clustering in A, cells were labeled by their independently determined cell identity, showing groupings by both developmental stage (e.g., QC region) and radial cell identity. Arrows indicate differentiation stage from young to older (top) inner to outer cell files (bottom). (C) Aggregate expression of genes enriched in either the epidermal or stele-endodermis-cortex G1 branch, which showed genes with differential functions. (D) UMAPs showing the expression of genes specific to sub-regions of the G2/M branch, with representative genes involved in cytokinesis (lower branch) and the G2/M transition (upper branch). (E) Variable lengths of G2/M phase marker expression shown within and between cell types, with representative time-lapse montages of the entire late G2/M period shown indicating duration. Red = HTR13 and yellow = CYCB1;1. (F) Quantification of G2/M duration for many cells. Asterisks represent significant differences in G2/M duration (pairwise t-test, $p < 0.05$). See also Figure S6, Table S3, and movie S1.



527

528 **Figure 3: The G₁ phase of the cell cycle is dramatically truncated in regenerating cells.** (A) Summary of
 529 the frequency of a given cell cycle phase in regenerating (yellow) and non-regenerating (grey) cells. Cells are
 530 aligned along a cell cycle pseudotime on the x axis, with their density shown on the y axis with G₁ predominant
 531 in non-regenerating cells and almost absent in regenerating cells. (B) Quantification of the coordinated G₁ exit,
 532 showing the coordinated depletion of cells in G₁ phase around 6 hours post-ablation (HPA) highlighted by grey
 533 shading. (C) Representative images of the coordinated G₁ exit (bottom). S-phase cells (top) serve as a control
 534 showing a continuous strong signal (no depletion) in the same roots. (D) Quantification of G₁ duration in
 535 control and ablated roots for two trials. Time is normalized within each root. Filled dots represent cells in which
 536 the end of G₁ was observed. (E) Representative time-lapse series of a short G₁ in which cells pass through
 537 the phase in as little as 2 hours. (F) Representative image of WIP4 expression domain before ablation and 24
 538 HPA. The purple wavy line marks the location of the ablation. (G) Quantification of WIP4 signal over time in G₁
 539 and S phase cells, with different plots showing analysis of cells grouped by the length of G₁ or S. H.
 540 Quantification of G₁ duration in two roots (left) and the timing of PET111 expression establishment in the
 541 regeneration zone in the same two roots (right) showing the association between G₁ duration and PET111
 542 appearance. Trials refer to individual root time lapses. See also Figure S7, Table S4-S5s, and Movies S2-S3.



543

544

545

546

547

548

549

550

551

552

553

554

Figure 4: Regenerating cells import glutathione to the nucleus in G1. (A) Representative confocal microscopy image of a PlacCI seedling stained with blue CMAC overnight, showing phase markers and blue CMAC staining. (B) Quantification of blue CMAC in G₁ and S phase nuclei. (C) Images showing the location of cells analyzed in 4D annotated (circles) and show in insets. All cells in these images were analyzed in 4E. (D) Representative images of cells in each phase of the cell cycle in control and ablated roots shown in a time-series montage. (E) Quantification of the cumulative change in blue CMAC levels in nuclei of cells in each cell cycle phase in a control or an ablated root over time. Time 0 is the beginning of the time lapse, and the time of the ablation is shown in the right panel as a wavy purple line. Image frames were taken three minutes apart. The blue peak in ablated cells at 10 minutes shows G₁ cells in the ablation time lapse experience a temporary increase in blue CMAC staining levels (GSH nuclear localization). See also Figure S8-S10 and Movie S4.

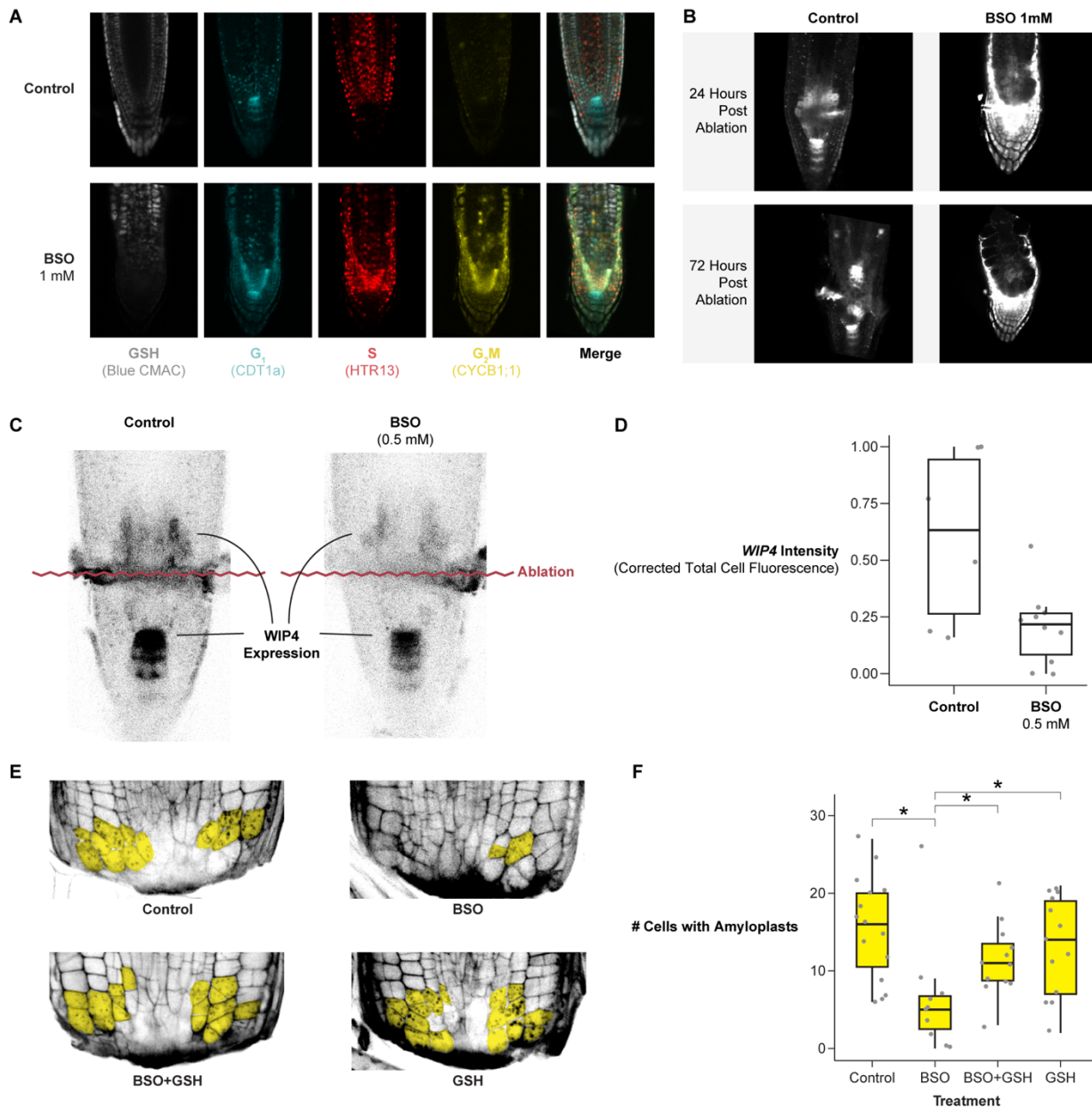
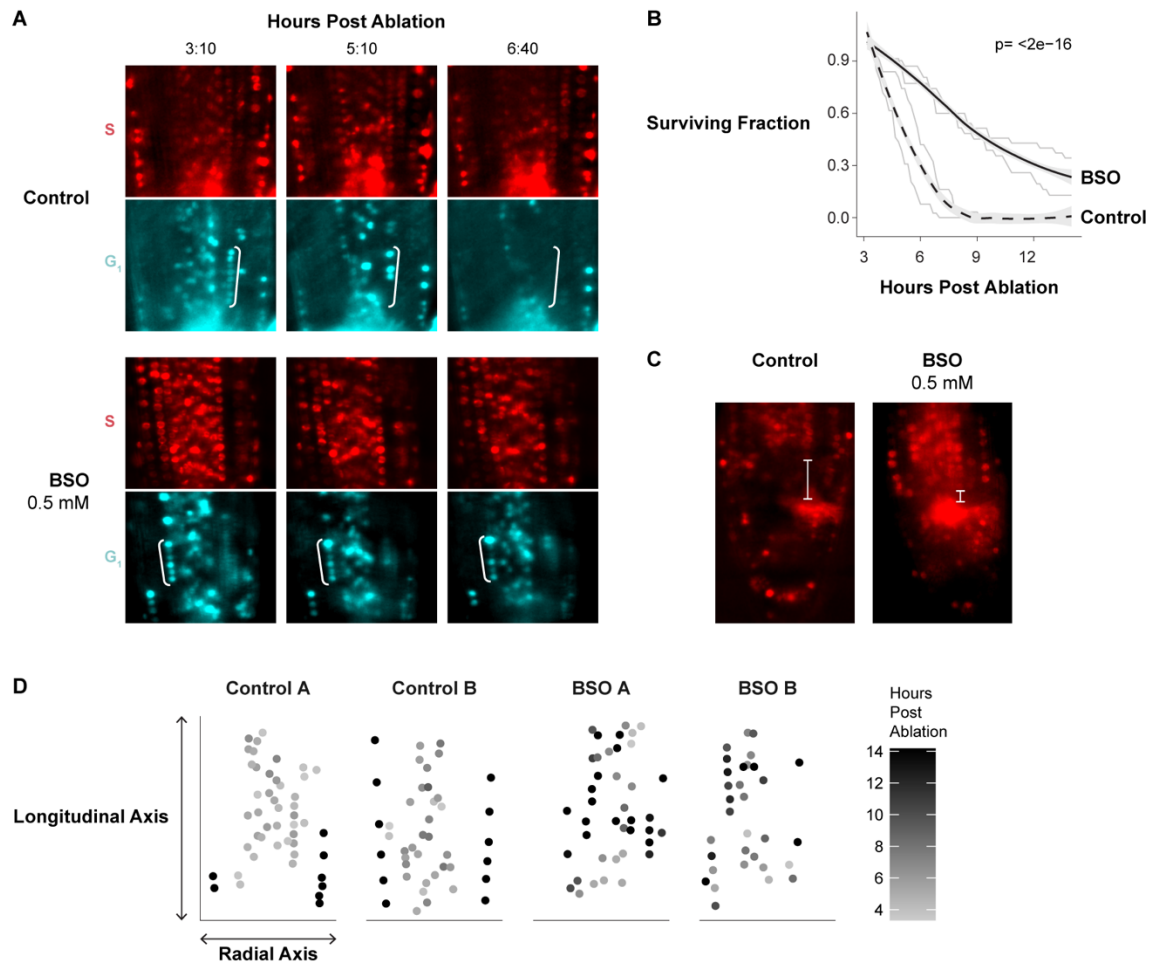


Figure 5: Depletion of GSH biosynthesis with BSO impairs regeneration and is rescued by exogenous GSH. (A) 7 days post germination (DPG) seedlings (PlaCCI x WIP4) grown on MS (control) or germinated on MS+1mM BSO then stained overnight with blue CMAC. (B) Representative images of the WIP4 signal in a median section of a control and BSO-treated root at 24 and 72 HPA. (C) Representative images of WIP4 signal 24 HPA in control and 0.5 mM BSO treatment. (D) Quantification of WIP4 signal in the regeneration zone of roots 24 HPA in control and 0.5 mM BSO treatment. The y-axis is the scaled corrected total cell Fluorescence. (E) Representative images of regenerating root tips stained with mPS-PI to visualize cell walls and amyloplasts 18 HPC. Cells with amyloplasts are pseudo-colored in yellow. The treatments are control, 0.5 mM BSO, 0.5 mM GSH, or combined 0.5 mM BSO + 0.5 mM GSH. (F) Quantification of the number of cells with amyloplasts in a population of roots from each treatment group shown in E. Pairwise statistical testing was performed using the Wilcoxon test.



567

568

569

570

571

572

573

574

575

576

577

578

579

580

581

Figure 6: Depletion of GSH with BSO eliminates the coordinated exit from G1 and increases G1 duration in regeneration. (A) Representative images from a control (upper) and BSO treated time lapse immediately shootward of the ablation site, showing the S phase (red) and G1 (cyan) markers. Cells from the cortex in G1 are bracketed to highlight the differential disappearance of G1 phase cells in control vs. post ablation. S phase cells are shown to confirm no change in their fluorescent signal. (B) G1 duration quantified in survivor curves, where cells in G1 were identified in the first frame of the time lapse and tracked until their transition to S phase for control (dashed line) and BSO-treated (solid line) time lapse experiments. Lightly colored lines are individual replicates, and the bold line is a LOESS regression of the two trials. P-value of survival rates is significantly different between control and BSO using the log rank test. (C) Images from the 24 HPA timepoint showing a marker for newly formed columella cells by measuring the proximal/distal range of expanded cells (characteristic of columella, white bracket). (D) Time that cells exit G1 mapped onto the given cell's coordinates within the roots, where the Y-intercept represents the ablation site and each dot represents a cell with two example roots per condition (A,B). Shading scale represents time post ablation when a cell exited G1 phase.

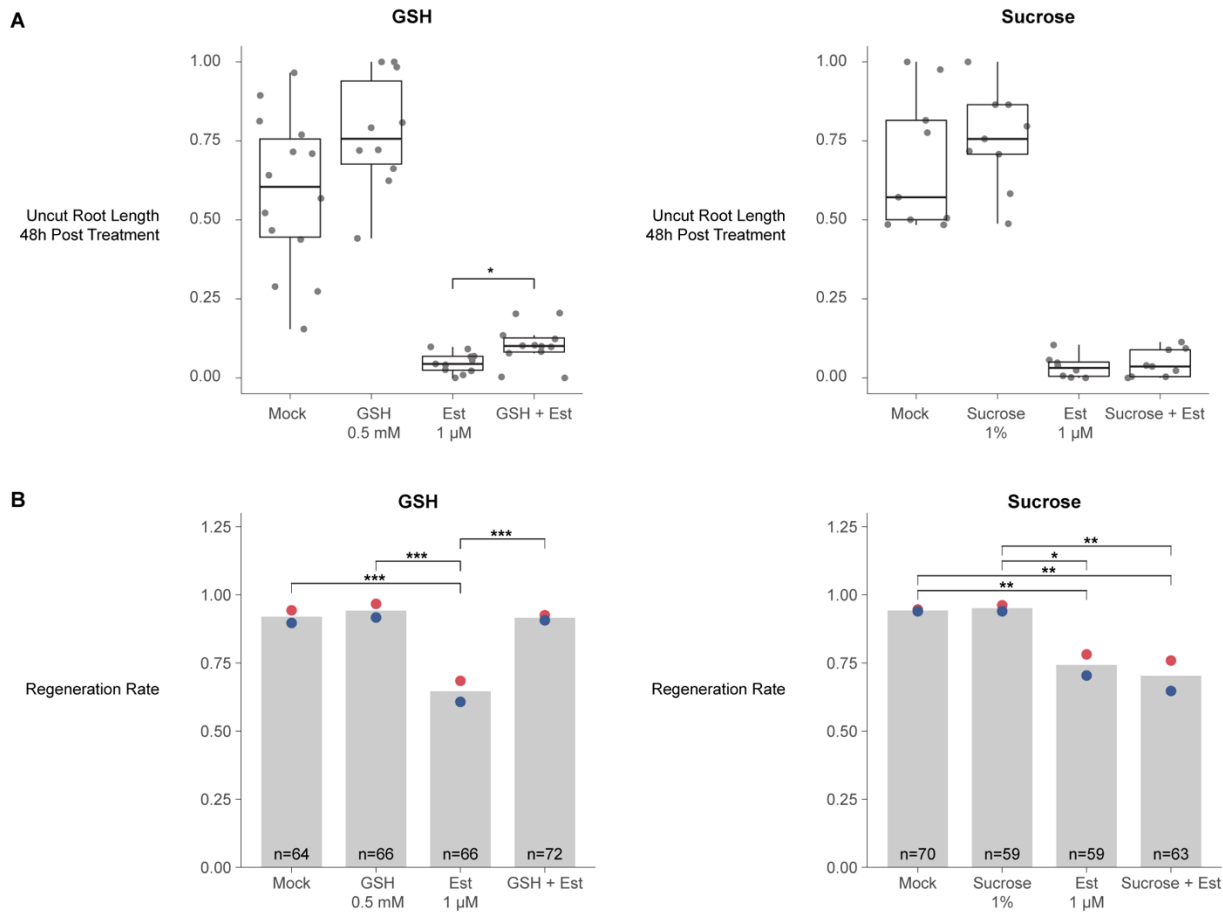
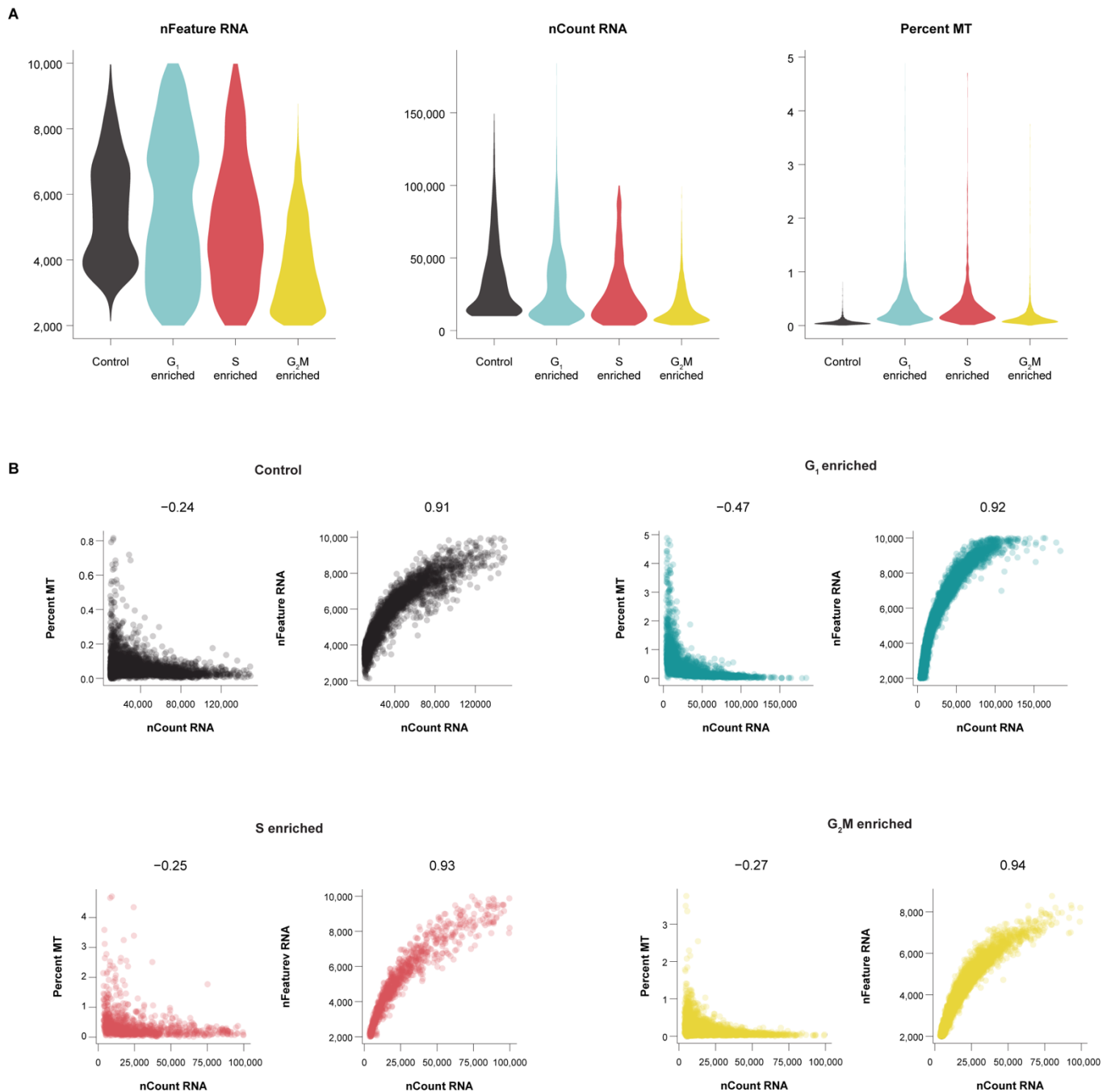


Figure 7: The ground tissue is a source of GSH in homeostatic growth and regeneration. (A) Root growth post callose-synthase induction for each treatment condition. Root lengths are scaled from 0 to 1 within technical replicates to their own controls to render them comparable across batches. Statistical significance was determined by the pairwise t-test comparing estradiol or non-estradiol categories (i.e. mock was tested versus GSH and estradiol was tested versus estradiol + GSH). (B) At left, regeneration rates based on the gravitropism test at 48 HPC. The conditions are control (mock), GSH treated roots, estradiol-treated roots (induction of callose synthase expression to block transport out of the cortex and endodermis), estradiol + GSH treated roots. At right, the same treatments substituting 1 μM sucrose for GSH. Red and blue dots represent the regeneration rates of technical replicates.

592

Supplemental Figure Titles and Legends



593

594

595

596

597

598

599

Figure S1. Single Cell RNA-seq Profiles Show Robust Signals in Quality Control; Related to Figure 1.

(A) Violin plots showing the number of genes (nFeature_RNA), RNA molecules (nCount_RNA), and the percentage of reads from mitochondrial genes (Percent_MT) per cell in each scRNA-seq library. (B) For each library, a pair of scatter plots shows (1) the anti-correlation between percent mitochondrial reads and number of RNA molecules detected (at left), and (2) the correlation between the number of genes and the number of unique RNA molecules detected (at right). Correlation coefficient is shown above the plot.

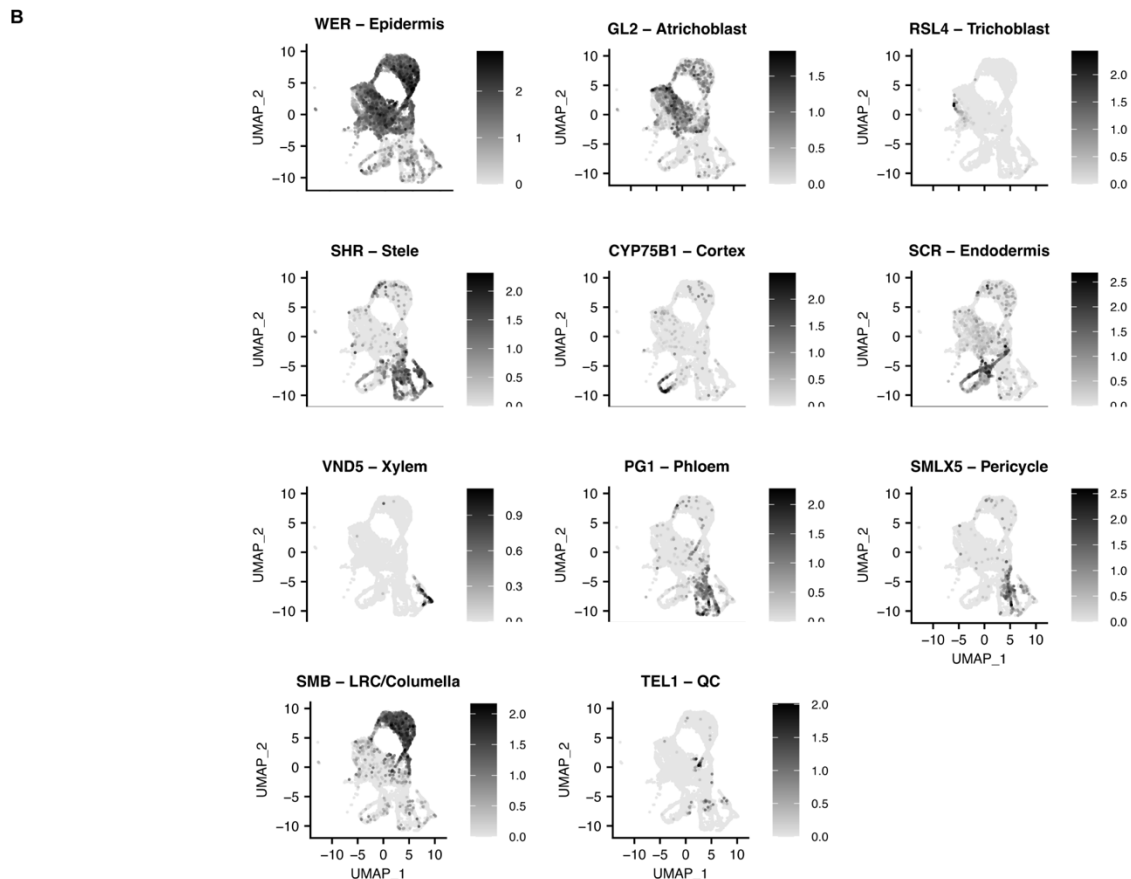
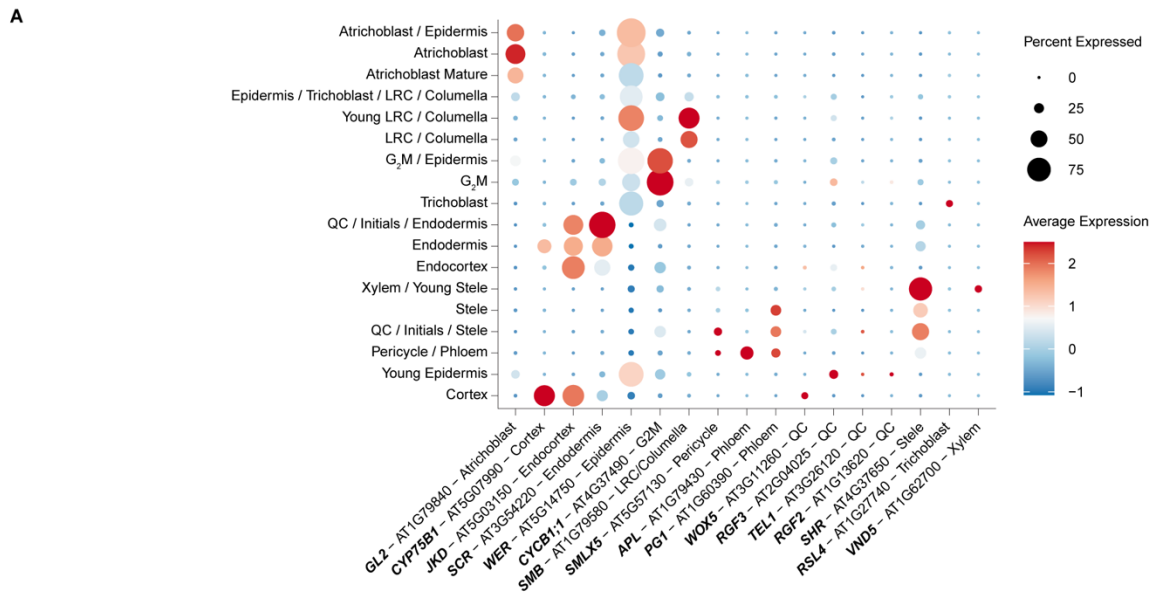
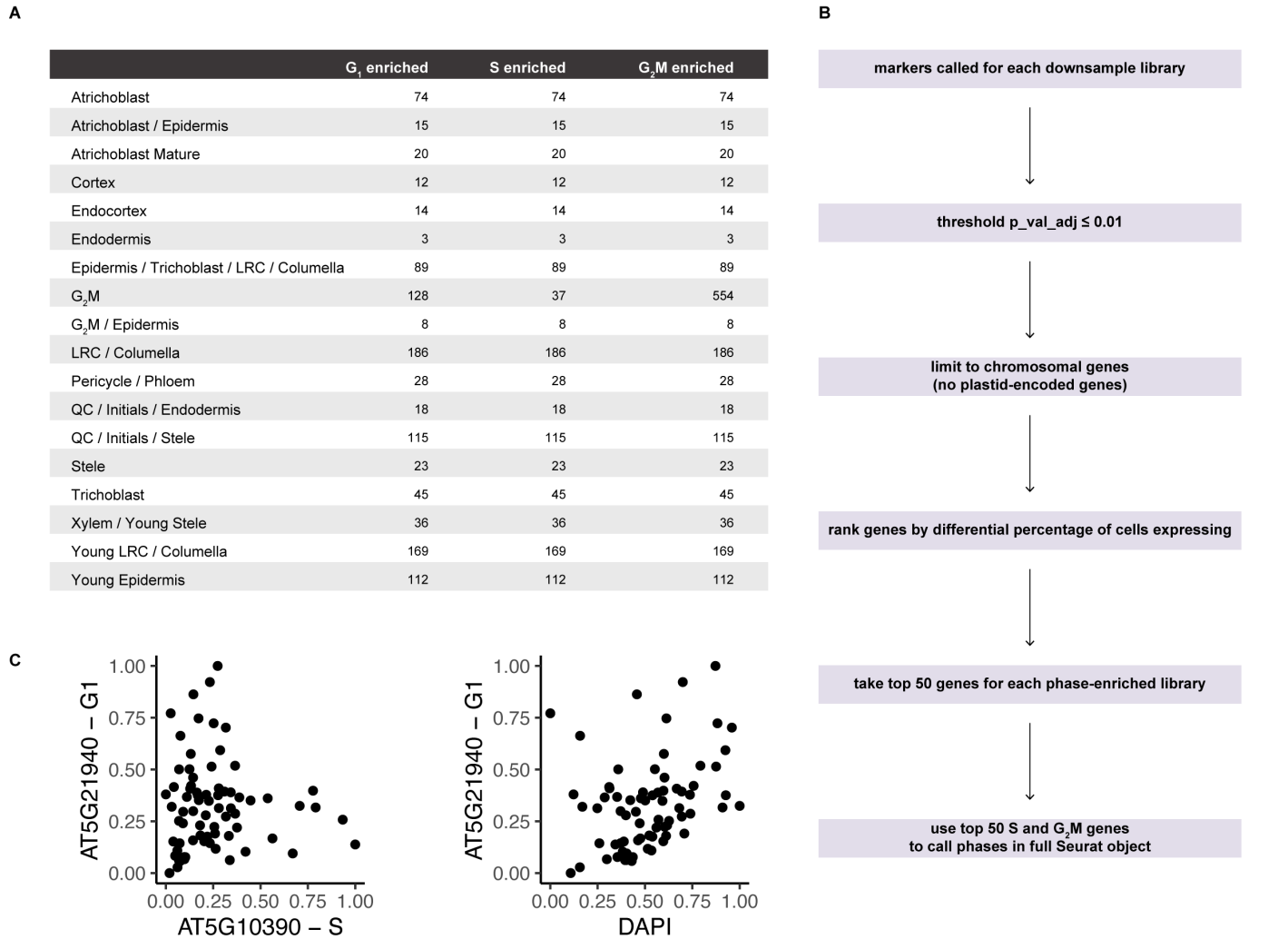


Figure S2: Markers robustly identify cell types in phase-enriched libraries, Related to Figure 1. (A) A dot plot showing the expression of marker genes across clusters defined by cell type in the integrated phase-enriched libraries. Size of the dot shows the percentage of cells in a cluster expressing the marker and the colormap shows the average expression of the marker in the cluster. (B) UMAPs highlighting the highly localized expression of various cell-type specific marker genes, as expected for robust capture of cell identities in scRNA-seq profiles.



607

608

609

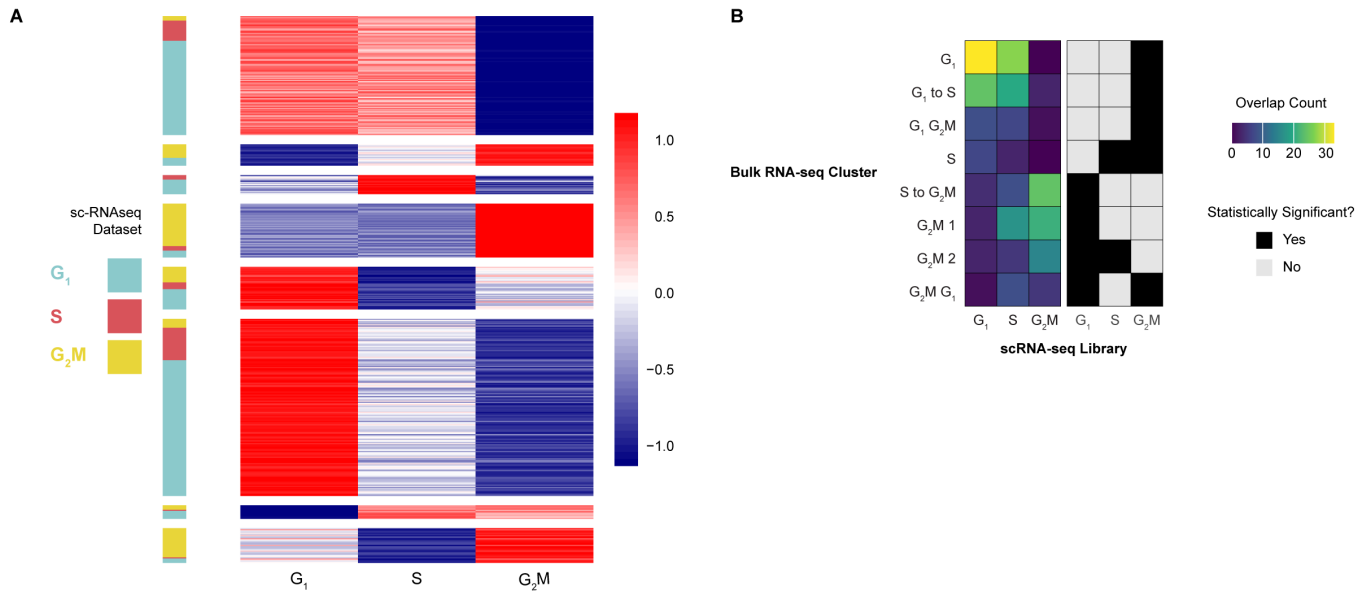
610

611

612

613

Figure S3. Data analysis methods identify cell phase markers with *in situ* validation of a new G1 marker; Related to Figure 1. (A) Cell counts for down-sampled phase-enriched libraries, ensuring a cell type contributed an equal number of cells to phase enrichment analysis and each cell type contributed to phase enrichment analysis. (B) Differential expression analysis pipeline to identify phase markers. (C) Anti-correlation between the G1 HCR probe and S-phase probe (left) and control plot showing G1 probe and DAPI signal with no anti-correlation (right).



614

615

616

Figure S4: Bulk RNA-seq profiles of the cell cycle confirm phase-enriched scRNA-seq; Related to Figure 1.

617

618

619

620

621

622

623

624

(A) Gene expression heatmap (red and blue) in which each row is a gene and each column represents the average expression profile across bulk RNA-seq profiles. Cells were sorted by phase using FACS to determine cellular ploidy level. The color bar to the left indicates which phase-enriched scRNA-seq library a given gene was upregulated in. Genes are grouped into 8 k-means clusters. High overlaps are shown for G1 and G2/M, while S-phase is not well defined in the ploidy sorting (B) Heatmaps showing the number of overlapping genes (left) and the statistical significance of the overlap (right) between differentially expressed genes from phase-enriched scRNA-seq (columns) and gene expression clusters of ploidy-sorted cells determined by k-means clustering (rows). Yes=statistically significant overlap at $p < 0.05$. See also Table S4.

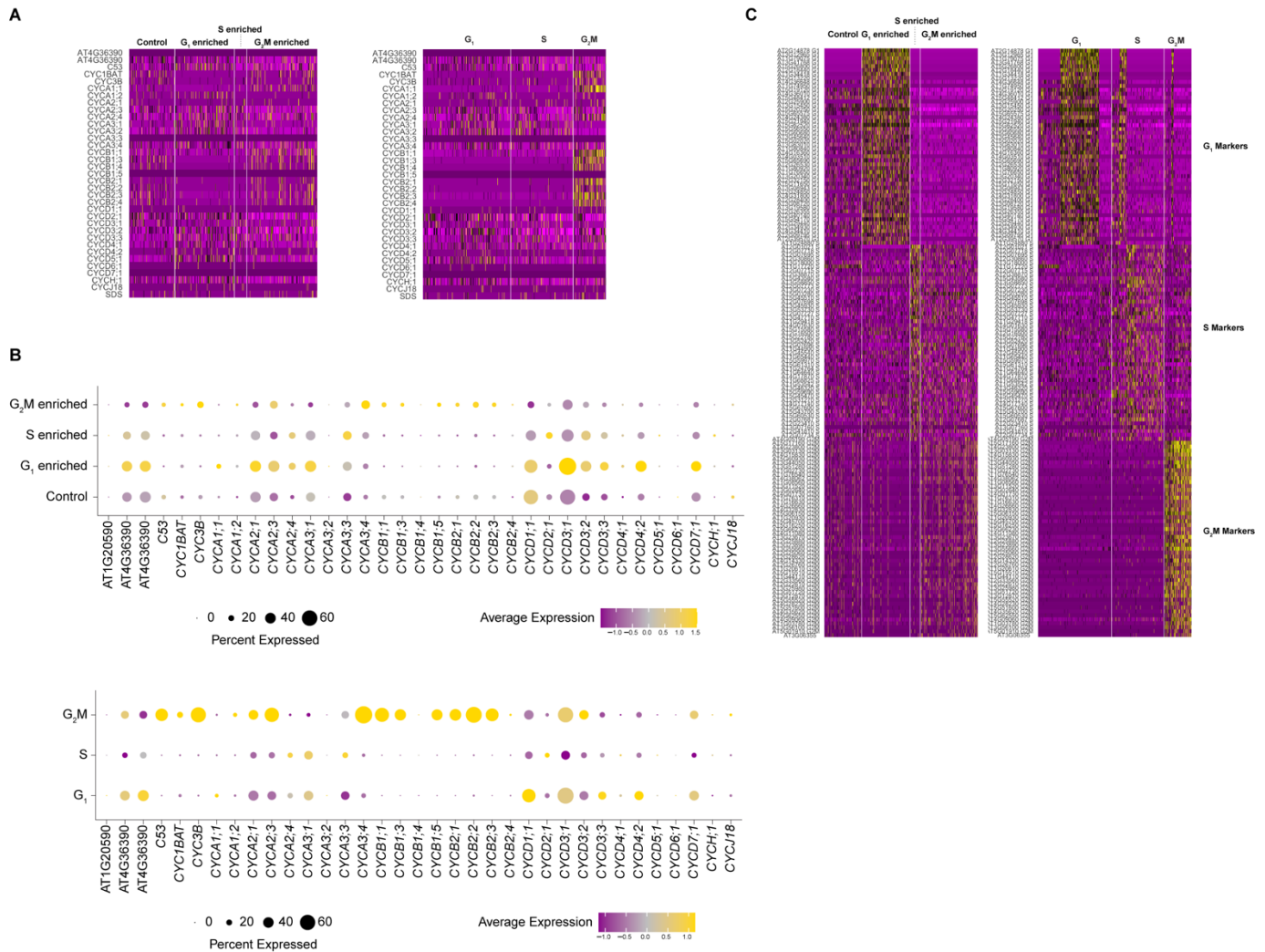


Figure S5: Enrichment analysis for phase markers shows agreement with known cell cycle markers but identifies more robust markers; Related to Figure 1. (A) Heatmaps comparing expression of classical cell cycle markers (rows) in cells (columns) grouped by the phase enrichment library from which they came (left) vs. cells assigned to phase based on marker analysis (right). At left, some enrichment of markers is visible but phase enriched libraries still contain cells in the non-target phase. At right, enrichment of known markers is more prominent when cells are grouped by our analysis pipeline, which is independent of the expression of the classical cell cycle markers. (B) A summary analysis of the heatmap data in A. Dotplots show the expression of cyclins in phase-enriched libraries (top) vs. phases assigned with our top marker genes (bottom). Cyclins are expressed in the appropriate datasets despite their sparseness (top). Cyclin expression behaves well based on phase assignments performed with our marker genes (bottom). (C) Following the same comparison as in A with the top 50 markers assigned by our pipeline. At left, the markers are shown based on their enrichments in the different phase libraries. These agree with classical markers but the analysis shows the new markers have higher expression and are more frequently detected in single-cell profiles. At right, the analysis show cells grouped into now phases using the top 50 markers. Note that many G₁-phase markers also express in early S phase, but S-phase has distinct markers to separate G₁ and early S.

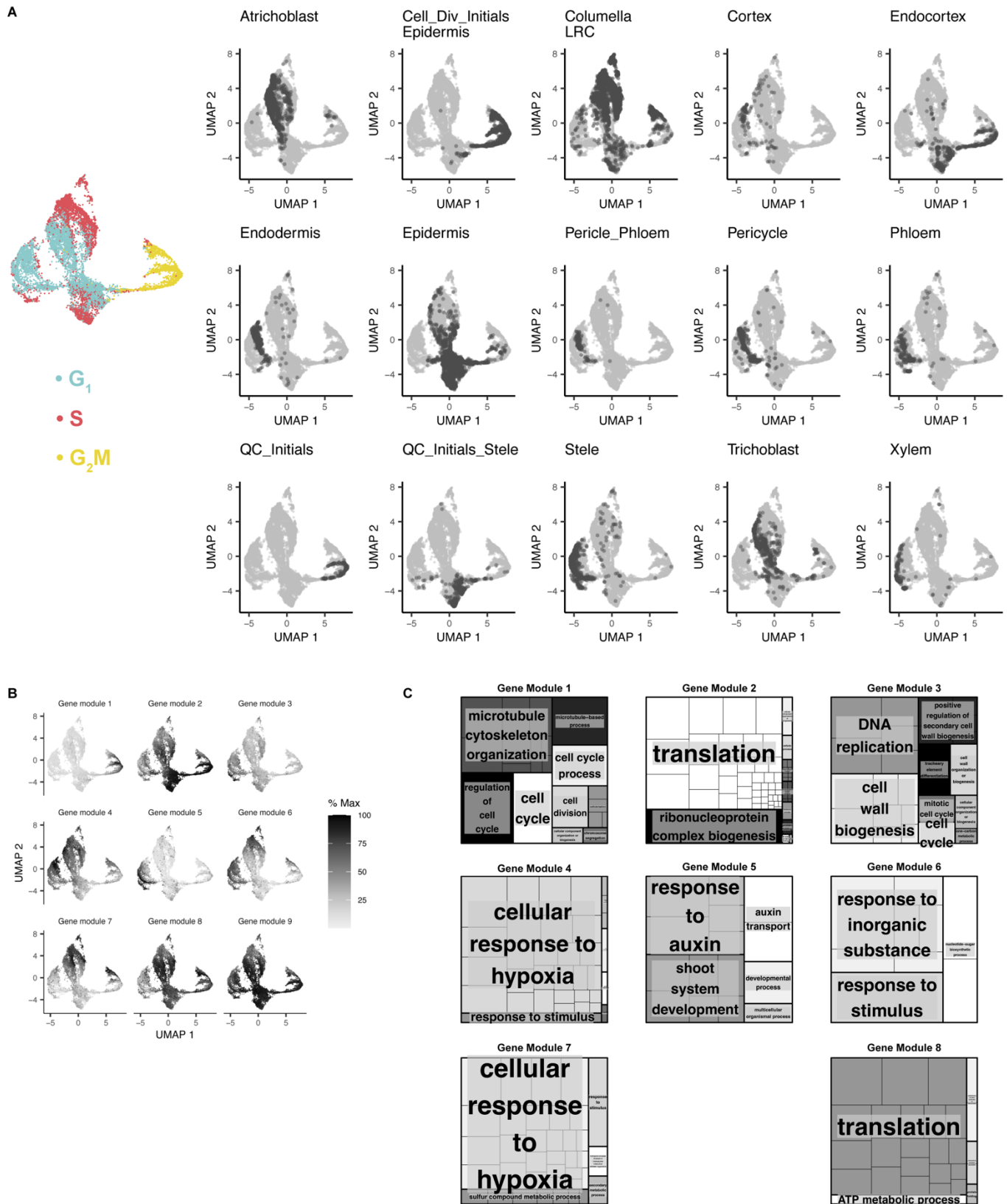
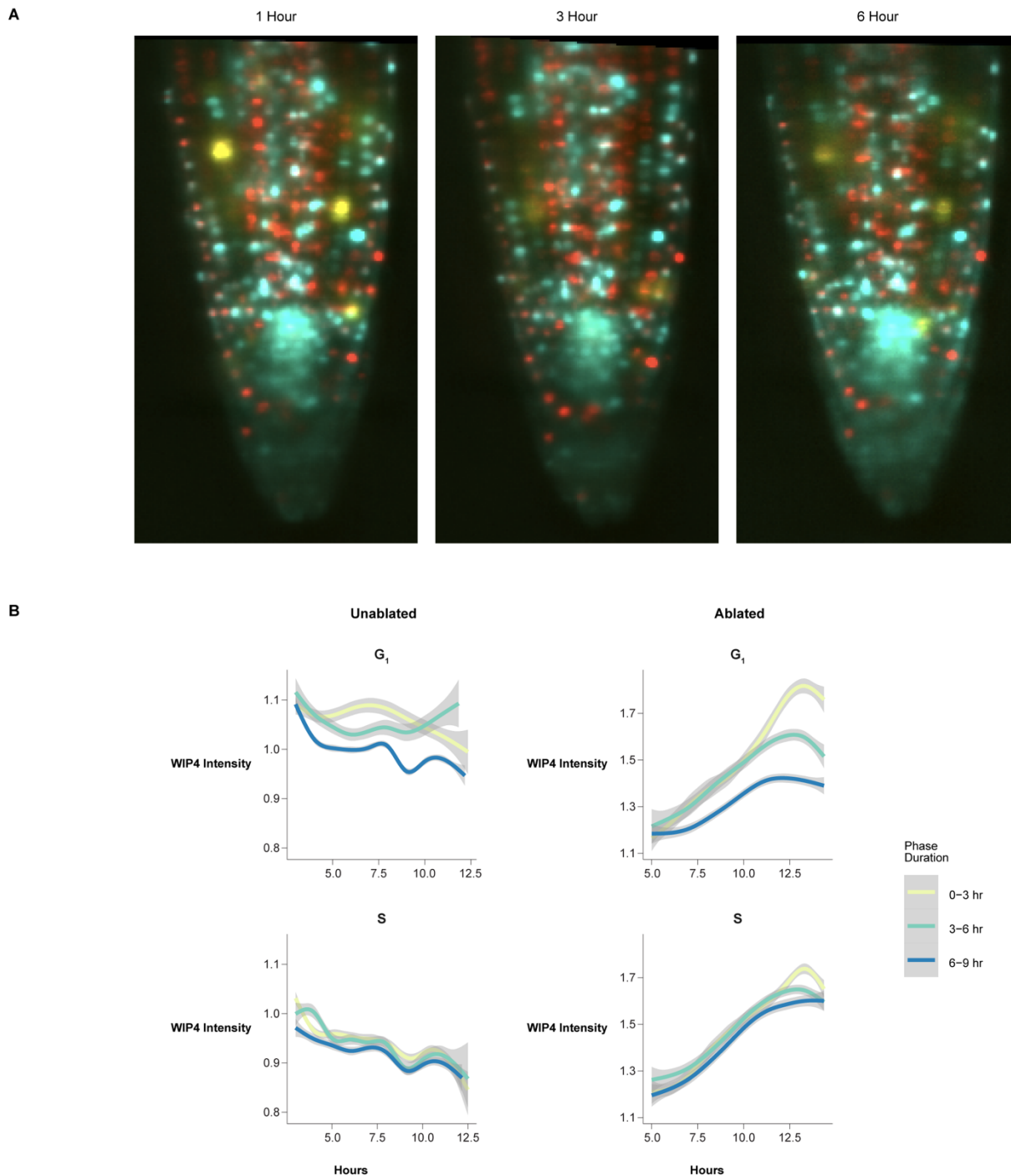


Figure S6. Cells of the same identity group together even when clustered by only cell cycle markers; **Related to Figure 2.** (A) UMAP outputs of pseudotime analysis clustered using the top 50 cell-cycle markers with an independent analysis of cell identity mapped onto the UMAP trajectories. In each panel, a different cell type is highlighted in black. At left, the cell cycle classifications are shown. (B) Analysis of gene modules that are preferentially expressed in dominant intervals along the pseudotime ordering, as determined by Monocle3

641
642
643
644
645
646

647
648
649

(see Methods). Grayscale shows the aggregate gene expression of each gene module. (C) GO-terms associated with the corresponding gene module shown in B. No significant GO terms were found for gene module 8.



650

651

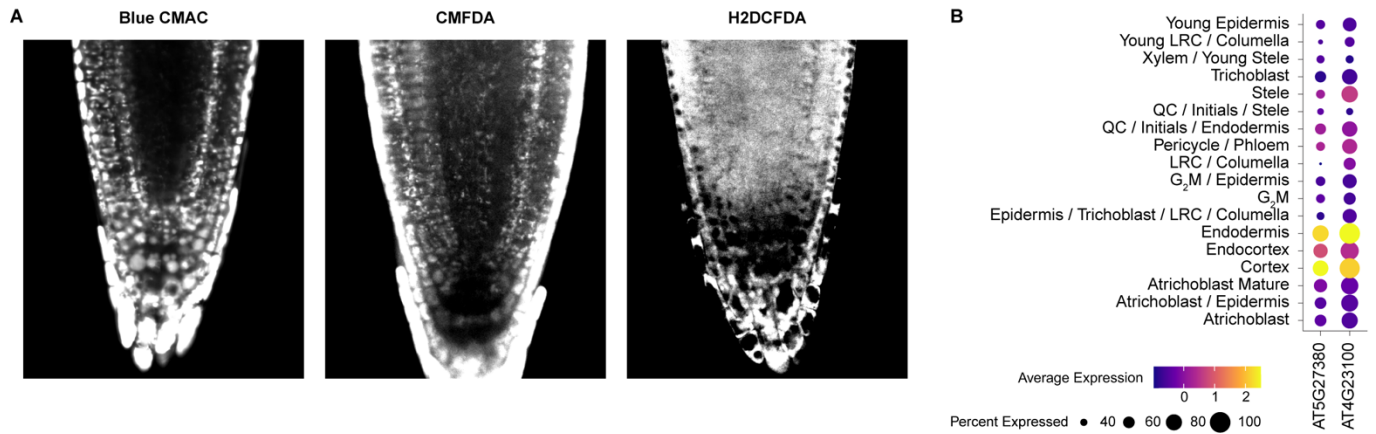
652

653

654

655

Figure S7: The appearance of newly reprogrammed cell identity correlates with rapid G_1 phases; Related to Figure 3. (A) Representative images of a control root expressing PlaCCI and WIP4::GFP at 1, 3, and 6 hour time points during a time-lapse acquisition. (B) Quantification of the WIP4 signal intensity in CFP+ and mCherry+ cells over the duration of time-lapse movies. The figure represents the complete analysis of data shown in Figure 3E.



656

657

658

659

660

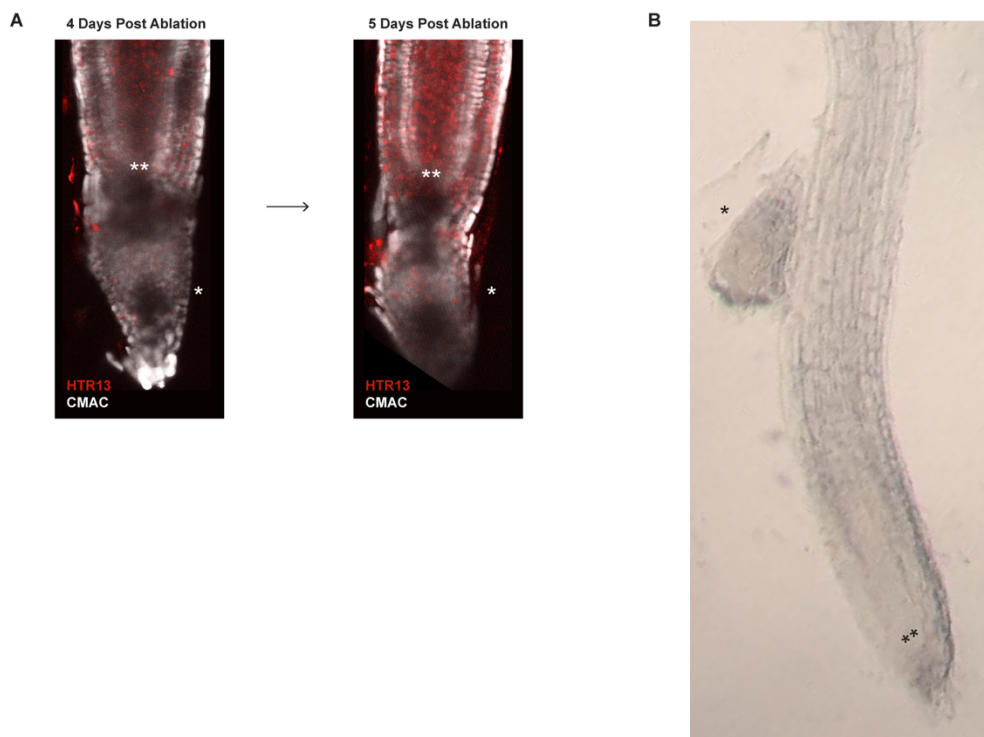
661

662

663

664

Figure S8. ROS and GSH dyes show different tissue localization patterns; Related to Figure 4. (A) Representative confocal microscopy images of seedlings stained for GSH (blue CMAC, CMFDA) or ROS (H2DCFDA) under control conditions. Note that the two GSH dyes agree and show prominent ground tissue staining. Note that CMFDA and H2DCFDA, with similar chemical structure but different target molecules, show different staining patterns. (B) Expression of GSH1 and GSH2 represented as dot plot derived from scRNA-seq profiles in different root cell types. Note the prominent expression in endodermis and cortex, in agreement with the GSH dyes.



665

666

667

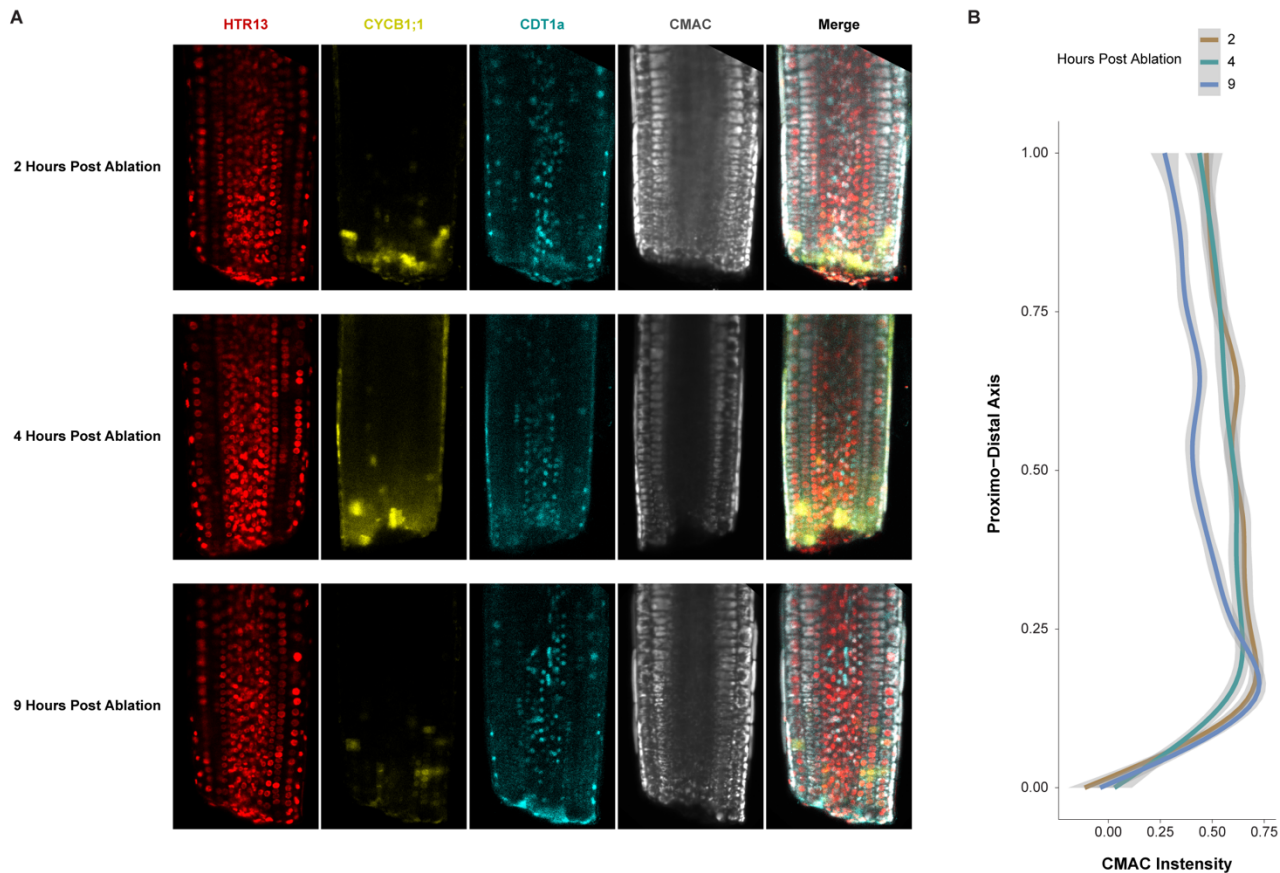
668

669

670

Figure S9. Transverse ablation leads to the reformation of a new root tip similar to the root tip excision procedure; Related to Figure 4. (A) Representative confocal images of seedlings (grown on standard 1/2 MS and then mounted in an imaging cuvette) undergoing regeneration. Between days 4 and 5 post-ablation it becomes apparent that new columella above the ablation is established proximal (shootward) to the original

671 QC (*), which is below the ablation. The tapered root cap, which includes the columella, is apparent distal to
672 the new QC (**), both of which are above the ablation site. (B) At a later time point, the original root tip (*) is
673 sloughed off as growth continues from the new QC/stem cell niche (**) in the same seedling shown in the lower
674 panel of A.



675 **Figure S10.** GSH dye CMAC is brightest in the same region where cells undergo rapid division and
676 **shortened G1 during regeneration; related to Figure 4.** (A) Representative confocal images of PlaCCI roots
677 stained with blue CMAC. Images were taken 2, 4, and 9 HPC. (B) Quantification of nuclear CMAC staining
678 intensity along the proximal-distal axis at different time points after ablation. The y-intercept represents the
679 ablation site and the range of the y-axis represents the visible length of root imaged in the frame as shown in
680 A. Note the peak of CMAC intensity right above the cut site between 0.00 and 0.25 on the longitudinal axis of
681 the root (y-axis), which is highest at 2-4 hrs post cut and begins to dissipate above point 0.25 at 9 hrs.
682

683 **Methods**

684 **Resource Availability**

685 Lead contact

686 Requests for resources or plant lines should be addressed to the lead contact for this work, Kenneth Birnbaum
687 (ken.birnbaum@nyu.edu).

688 Materials availability

689 Arabidopsis lines generated for this work are available following publication upon request.

690 **Experimental Models and Study Participants**

691 Plant growth and treatment conditions

692 Arabidopsis Col0 seedlings were grown vertically in an incubator set to long day conditions on ½ MS media
693 unless otherwise noted. For HU treatment, seedlings were synchronized in one of three cell cycle phases as
694 previously described³⁶. Briefly, seedlings were grown until 6 DPG vertically on ½ MS on top of sterile mesh
695 (product #03100/32, ELKO Filtering Systems). Then seedlings were transferred to MS plates supplemented
696 with 2mM HU (product # H8627, Millipore Sigma). Various incubation times were used to synchronize cells in
697 different phases of the cell cycle as follows: 6 hours for S phase, 17 hours for G2/M, and 22 hours for G1.
698 Synchronization in each phase was confirmed via confocal microscopy using the PlaCCI reporter. For BSO
699 treatment, seedlings were germinated on MS media alone (control) or supplemented with 1 or 0.5 mM BSO
700 (product # B2515, Millipore Sigma) as previously described³¹. Seedlings were grown vertically on this media
701 until they were 7 DPG and then used for either imaging or regeneration assays. Regeneration assays were
702 performed by manually removing the distal-most 70 microns of the root tip using an ophthalmic scalpel
703 (product #72045-15, Feather Safety Razor Company). Roots were then allowed to grow while regeneration
704 was monitored by either staining for amyloplasts at 18 hours with mPS-PI⁵⁰ or by counting the proportion of
705 roots that had recovered gravitropism at 48 hours². PlaCCI seedlings were crossed to cell type reporters
706 including WIP4 (columella and QC) WOX5 (QC), and PET111 (mature columella).

707 **Method Details**

708 Confocal microscopy

709 Laser ablations that were sufficient to cause new meristem establishment (regeneration) were performed using
710 a Coherent Chameleon Vision II 2-photon laser on a Zeiss 880 Airyscan microscope. A 2-dimensional ROI was
711 specified using the Zeiss ROI manager in the Zen Acquisition Black software with the time series, bleaching,
712 and ROI modes enabled. This ROI targeted a transverse section of the root that was positioned approximately
713 10-20 microns shootward of the QC that spanned the entire medio-lateral dimension of the root with a
714 thickness of approximately 5-10 microns. The ablation laser was used at 710 nm at 100 percent power for 15
715 iterations. In order to ensure sufficient tissue damage was achieved to induce the root to establish a new
716 meristem, the ablation was performed in 3 Z planes: (1) in the medial plane, and then on both sides of the
717 medial plane (2) closer to the cover slip and targeting the epidermis and cortex (about 15-20 microns off the
718 medial plane), and (3) further from the cover slip than the median plane as deep as the confocal microscope
719 could image into the tissue before imaging quality degraded (15-20 microns from the medial plane). Each
720 ablation was performed as part of a time lapse acquisition, in which typically two frames were acquired,
721 followed by the ablation, and then three additional frames were acquired. These frames were set to be
722 acquired 1 millisecond apart, which functionally resulted in continuous acquisitions and total time lapses of
723 approximately 90 seconds. For 30-minute-long time lapses taken on the Zeiss 880 Airyscan confocal, frames
724 were acquired in one Z plane three minutes apart. This laser ablation strategy was adopted to enable imaging
725 of injured roots that were already mounted in a cuvette compatible with our light sheet setup (described below)
726 so that we could monitor injury response via time lapse microscopy without any confounding effects of the
727 stress of mounting seedlings after root tip removal.

728 Plants were stained with blue CMAC by mounting in imaging cuvettes as described above using media
729 supplemented with blue CMAC (ThermoFisher #C2110) to achieve a concentration of 10 µM once the media
730 had equilibrated to 30 degrees Celsius. Media was then split into a number of batches equal to the number of
731 treatment conditions to ensure that all conditions received the same concentration of blue CMAC. Additional
732 treatments were then supplemented into the relevant batch of media as required. 5 mL of each media

733 treatment was then added to its own cuvette and cured for at least four hours at 4 degrees Celsius. Plants
734 were then transferred to an imaging cuvette and allowed to recover in the growth chamber overnight.

735 Light Sheet Microscopy

736 Samples were mounted for light sheet microscopy as follows: plants were grown vertically on MS plates for 6
737 days. On day 6, 5 mL of MS with 2% low melt agarose was cast into imaging cuvettes (CellVis product number
738 #C1-1.5H-N) after being filtered through a 0.45 micron nylon filter (product # 76479-042, VWR) to remove any
739 particulates that might disturb the path of the light sheet to prepare media “blankets”. These blankets were
740 stored at 4 degrees Celsius for at least four hours prior to mounting to ensure they had fully polymerized. A
741 sterile scalpel and forceps were used to remove a small amount of media from one end of the cuvette to create
742 a gap that could be used to lift the media out of the cuvette. The scalpel was then gently run along the edge of
743 the imaging chamber to free the blanket while producing minimal distortions to the media. Sterile canted
744 forceps were then used to gently lift the media blanket out of the cuvette and placed in a sterile petri dish.
745 Several 6 DPG seedlings were placed on top of the media blanket such that the roots were in contact with the
746 blanket and the shoots hung off the edge. A fresh cuvette was then lowered over the blanket until the blanket
747 made contact with the cover slip at the bottom of the cuvette. Seedlings were inspected for tissue damage
748 under a brightfield microscope and any gaps between the blanket and the wall of the cuvette were filled in with
749 additional filtered media prepared as above to ensure the light sheet did not pass through any air gaps. The
750 assembled cuvettes were then placed into a growth chamber overnight oriented such that the roots pointed
751 downward to allow the plants to recover from the stress of the mounting procedure. Roots were then imaged at
752 7 DPG. Seedlings were imaged on an inverted Leica model Dmi8 outfitted with a Tilt Light Sheet Imaging
753 System (Mizar) with filters optimized to visualization of YFP, CFP, and mCherry (Chroma). Roots were imaged
754 with a 40X water immersion objective, with stacks spanning the entire Z dimension spaced 1.5 microns apart
755 acquired every ten minutes in mCherry, CFP, and YFP to create time lapse movies of PlaCCI. Laser power
756 and acquisition time was adjusted for each experiment to account for variable distance of the sample to the
757 side of the cuvette through which the light sheet enters. A sample binning of 2 was used to improve signal
758 brightness. For imaging of the F3 progeny of PlaCCI crossed to the WIP4 transcriptional reporter or the
759 PET111 enhancer trap line⁴⁸ in which both transgenes had been screened for stable brightness, a fourth
760 channel - GFP - was imaged. No photobleaching was observed using these imaging conditions over the
761 course of a time lapse. To maintain imaging quality, water was added to the 40X objective after 7-10 hours of
762 imaging depending on the ambient humidity. This was accomplished by briefly removing the imaging cuvette
763 between acquisitions, adding additional water to the objective, and then replacing the cuvette. The stage was
764 adjusted to recenter the sample and then the image was realigned *post hoc* using Imaris to account for any
765 subtle shifts in sample position. This allowed us to avoid moving the stage, which would necessitate adjusting
766 the focus of the light sheet midway through the time lapse acquisition.

767 scRNA-seq

768 Protoplasts were generated as follows: To collect roots enriched for different phases of the cell cycle, root tips
769 were synchronized with 2mM HU media as described above. To process cells synchronized in different phases
770 in parallel, seedlings were transferred to HU media in a staggered manner such that they would be ready for
771 harvesting at the same time.

772 The distal-most 400 μ m of approximately 500 root tips were excised from 7 DPG seedlings and then collected
773 via capillary action with a P200 pipette tip containing 25 μ L of protoplasting buffer. These root tips were then
774 dispensed into cell wall degrading solution as previously described⁸². Root tips were gently agitated on an
775 orbital shaker for approximately 1 hour and were gently pipetted up and down with a P1000 pipette every ten
776 minutes after the first half hour of incubation. Root tips were then passed through a 40-micron cell strainer

(product # 08-771-1, Fischer Scientific) and any large aggregates of cells were gently pressed against the strainer using sterile flat forceps to release any cells that had so far failed to dissociate.

10X libraries were prepared from protoplasts to generate scRNA-seq libraries using the Chromium Next GEM Single Cell 3' Reagent Kit v3.1 (10X Genomics) following manufacturer's instructions.

The cDNA and sequencing library fragment sizes were both measured with the Agilent TapeStation 4200 using the high sensitivity 1000 (product # 5067-5582, 5067-5583) and 5000 (product # 5067-5592, 5067-5593) reagents respectively. Sample concentration was detected using the Qubit HS dsDNA (product # Q32851, Thermofischer) assay following manufacturer's instructions. Library quantitation for pooling was performed as follows: the fragment size and concentration of the library in ng/μL were used to determine the molarity of the libraries with the following equation: $[\text{Lib Conc (ng/}\mu\text{L)}]/[(\text{Frag Length (bp)} * 607.4)+157.9] * 1000000$. Libraries were then diluted to 3 nM concentration and pooled for sequencing. Samples were sequenced on a Novaseq 6000 using an SP flowcell in 28x91 paired end 100 cycle mode with V1.5 reagents (100 cycles).

Bulk RNA-seq

For bulk RNA-seq, total RNA was extracted from sorted protoplasts using the Qiagen RNA micro kit following manufacturer's instructions. RNA quality was determined using RNA high sensitivity reagents (product # 5067-5579, 5067-5580, 5067-5581, Agilent) for the Agilent TapeStation 4200. Total RNA was used to synthesize cDNA using the SMART-Seq v4 full-length transcriptome analysis kit from Takara (product # 634888) using protocol B specified in the manual on page 12. The quality of cDNA was then assessed using D1000 reagents for the Agilent TapeStation. The resulting cDNA was used to generate sequencing libraries with the Ovation Ultralow Library System V2 from Tecan (product # 0344) following manufacturer's instructions. Libraries were then sequenced on a Novaseq 6000 with an SP flowcell in 1x100 single end 100 cycle mode with V1.5 reagents (100 cycles).

Cells were collected by FACS as follows: Root protoplasts were sorted using a BD FACS Aria II using FACS Diva software as described previously^{83,84}. Briefly, protoplasts were sorted directly from cell-wall degrading solution into a 1.5 mL microcentrifuge tube containing 350 μL of Qiagen RNA extraction buffer supplemented with beta mercaptoethanol.

Protoplasts expressing an H2B RFP fusion and a CDT1a GFP fusion under the native promoter were sorted and gated to remove doublets and debris. Then RFP positive events were identified by plotting red scale autofluorescence versus RFP and then gating for cells that showed RFP fluorescence above background as defined by a Col-0 control expressing no fluorescent proteins. In tandem, CDT1a positive cells were identified by plotting autofluorescence versus GFP and gated for GFP expression above background relative to Col-0 control. Then both the RFP+ and GFP+ populations were plotted in a histogram of RFP signal v. cell count. This revealed a population with two RFP peaks characteristic of DNA staining in dividing cells. The GFP+ population (CDT1a reporter fluorescence) overlapped with the 2n ploidy peak, which is consistent with its expression in the G1 phase of the cell cycle and was used as a positive control. Further gates were defined based on the histogram to collect cells in G1 (2n), G2/M (4n), and S (intermediate RFP signal) phases. These populations were collected simultaneously in a three-way sort and the maximum number of cells were collected for each phase. This protocol was repeated independently twice to generate 6 samples for RNA-seq library preparation. Samples were snap frozen and stored at -80 degrees Celsius until all samples were collected and could be processed for RNA extraction and library preparation simultaneously.

In order to use cellular ploidy as a proxy for cell cycle phase, it was critical to harvest the distal-most portion of the root tip in order to avoid harvesting any cells that had already begun endoreduplication. The distal-most 200 μm of approximately 500 root tips were excised from 7 DPG seedlings and then collected via capillary action with a P200 pipette tip containing 25 μL of cell-wall degrading solution. These root tips were then dispensed into cell-wall degrading solution. Root tips were gently agitated on an orbital shaker for

822 approximately 1 hour and were gently pipetted up and down with a P1000 pipette every ten minutes after the
823 first half hour of incubation. Root tips were then passed through a 40-micron cell strainer and any large
824 aggregates of cells were gently pressed against the strainer using sterile flat forceps to release any cells that
825 had so far failed to dissociate. The resulting protoplasts were then transferred to a test tube appropriate for the
826 cell sorter and immediately processed via FACS.

827 Sequencing Data Analysis

828 *Bulk RNA-seq*

829 For Bulk RNA-seq, reads were trimmed using Trimmomatic version 0.39 in single end mode with the following
830 settings: ILLUMINACLIP:TruSeq3-SE:2:30:10 LEADING:3 TRAILING:3 SLIDINGWINDOW:4:15 MINLEN:36.
831 Trimmed reads were mapped to the Arabidopsis TAIR10 genome using HISAT2 version 2.2.1. Reads mapping
832 to genes were counted with Rsubread (version 1.22.1) featureCounts in single end mode with a minimum
833 overlap of 5 and counting only primary alignments and ignoring duplicates. Reads were normalized using the
834 TPM calculation and the resulting count matrix was used to calculate mean values per condition, filtered to
835 remove genes with low expression and low variance, and then clustered via k-means clustering. The number
836 of k (8) was chosen to reflect the total permutations of expression changes (up or down) and cell cycle phases
837 (G1, S, G2/M).

838 *scRNA-seq*

839 For scRNA-seq the mkfastq function in Cell Ranger 5.0.1 was used to generate fastq files from the raw
840 sequencing output. Count matrices for scRNA-seq experiments were then generated with the count function
841 and the TAIR 10.38 release of the Arabidopsis genome.

842 *Quality Control – scRNA-seq*

843 After generating count matrices using Cell Ranger, Seurat was used to filter cells based on the number of
844 features detected (more than 2000 and less than 10000), percent mitochondrial reads (less than 5), and total
845 RNA molecules detected (less than 100000). This produced datasets in which the R squared coefficient
846 between features and counts exceeded 0.93, indicating that the remaining cells in the dataset were healthy
847 singlets. Libraries were integrated using the sctransform workflow in Seurat³⁷.

848 *Identifying Cell Cycle Markers*

849 Cell type annotations were carried over from a control dataset that had previously been annotated based on
850 the expression of cell type specific marker genes. Cell labels were carried over manually by examining the
851 cluster membership of cells from the control library, which formed the same stable clusters as they had in
852 previously when integrated with this dataset. Previous cluster identity was then manually transferred to all cells
853 from the HU-treated datasets that shared cluster membership with the annotated cells from the control dataset.

854 Transcriptional detection of phase enrichments for scRNA-seq libraries were validated by comparing
855 upregulated genes in each scRNA-seq library with expression patterns in ploidy-sorted bulk RNA-seq. Due to
856 the absence of a clear peak for S phase, we collected many fewer cells from S-phase. Thus, we did not expect
857 a high overlap in this phase. However, phase agreements were high in both G2/M and G1 phases, validating
858 the synchronization method. For S phase, upregulated genes in the enriched scRNA-seq libraries were
859 enriched for functions already known to be core for S-phase including many histones. Thus, we used the
860 scRNA-seq to generate markers because of its high resolution of each phase.

861 While the scRNA-seq libraries were enriched for cells in each phase of the cell cycle, their cell type
862 composition was variable. To ensure the identification of cell cycle markers present in all cell types, we

863 projected them on the same UMAP space, determined the lowest number of each cell type across all enriched
864 libraries and then randomly down sampled each cell type in each library to produce libraries with equal cell
865 type composition. We then performed differential expression analysis with cells from each phase enriched
866 library using Seurat's FindAllMarkers function. Markers were ranked by percent differential expression and the
867 top 50 for each library were chosen as cell cycle marker genes. Markers were then used to analyze the cell
868 cycle in the full (not down sampled) scRNA-seq dataset and other non-synchronized scRNA-seq datasets.

869 *Pseudotime Analysis*

870 For cell cycle pseudotime analysis, Monocle3 was used to create the UMAP embeddings with the top 150
871 ranked genes for each phase of the cell cycle. We then used the learn_graph and order_cells functions to
872 calculate a pseudotime trajectory for cells based on the cell cycle. To find genes that changed as a function of
873 pseudotime we used the graph_test function. We then aggregated the gene expression matrix based on evenly
874 spaced bins along the pseudotime trajectory and clustered those bins based on gene expression to assign
875 genes to different positions in the pseudotime trajectory.

876 Data visualization was generated using ggplot2 with Tidyverse, Seurat, pHeatmap, Treemap and Monocle3.

877 Imaging Data Analysis

878 Long-term time-lapse images were registered in 3 dimensions by first detecting objects (either nuclei, WOX5,
879 or WIP4 expression) and then using detected objects to correct the reference frame for the time lapse in 3
880 dimensions. The new reference frame was then used to correct the time lapse for both translational and
881 rotational drift. Once drift corrected, nuclei were then segmented again using the spot detection tool. Once
882 segmented, statistics for all nuclei were exported to R for further analysis. Cell phase was determined by
883 measuring the amount of YFP, CFP and mCherry signal in each nucleus. If CFP or YFP signal exceeded a
884 detection threshold cutoff, cells were classified as G1 or G2M respectively. All other cells were classified as S
885 phase. The PlaCCI reporter does not easily distinguish between cells in S phase versus early G2, so it is
886 possible that some G2 cells were classified as S phase cells in this analysis. Counts of cells in G1 (Figure 3B),
887 G1 durations (Figure 3D), and G1 exit time (Figure 6B) were determined manually. The log rank test was used
888 to determine the significance of the G1 survivorship analysis^{85,86}.

889 For still images, 3-dimensional segmentation was performed in Trackmate by treating the Z dimension as a
890 time dimension. Nuclei were segmented based on the mCherry channel and then data for each channel within
891 nuclei was exported to R for further analysis.

892 Confocal image stacks were taken such that nuclei would appear in at least two consecutive slices. Therefore,
893 all nuclei that appeared in only one slice were discarded. For the remaining nuclei, Blue CMAC signal was
894 scaled from 0 to 1 per cell file to render nuclei comparable. In the case of short-term time lapses of PlaCCI
895 roots stained with Blue CMAC taken using confocal microscopy, drift was corrected in 2 dimensions using the
896 Correct 3D drift plugin in FIJI prior to Trackmate segmentation. Nuclei were filtered if they were not tracked for
897 the entire time lapse. Blue CMAC signal was calculated as a change over the value at time zero.

898 In Situ Hybridization

899 Probe selection - Candidate probes were selected from the top marker set described above if they had a were
900 expressed in at least 80 percent of cells from the target phase and if they exceeded a differential expression
901 threshold of 0.25 LFC based on a differential expression test performed in Seurat with the design. Then the
902 average expression for each gene in the marker set within a given phase was calculated. The top 5 most
903 highly expressed genes from each phase that had passed the differential expression filtering step were chosen
904 as candidates for further analysis. The expression of this small set of genes was examined manually to ensure
905 there was no cell-type-specific bias. Finally, the most strongly expressed candidates from this set were chosen

for probe design. Genes from these sets that had either unknown function or were not previously characterized as being cell cycle regulated were prioritized. Probe design was performed by Molecular Instruments. *In situ* hybridization was performed as described previously⁸⁷ with the minor modification of eliminating the proteinase K digestion to preserve the integrity of the Arabidopsis root for imaging.

Quantification and Statistical Analysis

For scRNA-seq statistical analysis, differential expression tests to identify markers were performed using Seurat in R and the results of that statistical test are reported in Table S1. For imaging and regeneration data, statistical tests are reported throughout the manuscript and are available in figure legends. All statistical tests were performed in R. Statistical tests for data comprised of count variables were performed using the Wilcox test implemented in the rstatix package. Where noted, count data was tested using the Chi-square test with the stats package. Statistical tests of data comprised of continuous variables was performed the rstatix using the pairwise t-test function. The log rank test was used to determine the significance of the G1 survivorship analysis^{85,86}. Loess regressions are shown throughout the manuscript with 95% confidence intervals calculated by the ggplot2 smooth function. Wherever n is less than 30, results are plotted as a combined box and jitter plot so that the n number is visible in the summary plot. Where n is greater than 30, the n value is annotated onto the summary plot.

Where fluorescence results are quantified, they are represented as the corrected total cellular fluorescence where the area of the relevant region of interest (ROI) was multiplied by the average fluorescence intensity of the background signal of the image. This value was then subtracted from the integrated density value of the ROI. Each of these values was obtained in FIJI using the measure function. ROIs were either determined manually based on the expression domain of a reporter gene, or were determined with automatic segmentation for all visible nuclei using either TrackMate or Imaris.

Gene ontology enrichments were determined using the gene list analysis portal in Thalemine.

Supplemental Table Titles and Legends

Table S1. Summary of all differentially regulated genes identified in this study; Related to Figure 1 and S1-S5. KmeansClust refers the cluster identified in S4. Sequencing method indicates which method the gene was detected in. sc_log2foldchange refers the log2 fold change in the scRNA-seq phase marker identification analysis. Similarly, sc_pval_adj, sc_phase, and sc_diffpct refer to the adjust p-value, enriched library, and difference in percent cells expressing in the same analysis. Marker indicates which phase a gene was identified to be a marker of for the top 50 markers. Permissive marker is the same, but includes the top 200 markers.

Table S2. Gold standard markers from prior transcriptional studies; Related to Figure 1.

Table S3. Gene Set Enrichment analysis results for the top 50 and top 200 marker sets as well as the G1 bulk RNAseq clusters; Related to Figures 1 and S4.

Table S4. Differential expression analysis of G1 subpopulations; Related to Figure 2.

Table S5. G1 duration summary; Related to Figure 3.

Supplemental Movie Titles and Legends

Movie S1. Time lapse movie showing G2/M duration during homeostatic growth; Related to Figure 2. Time stamp is shown in days:hours:minutes. CYCB1;1-YFP is shown in yellow.

Movie S2. Time lapse movie showing two replicates of PlaCCI crossed to WIP4 during homeostatic growth; Related to Figure 3. Time stamp is shown in days:hours:minutes. CYCB1;1-YFP is shown in yellow,

947 CDT1a-CFP is shown in cyan and HTR13-mCherry is shown in red. The CDT1a-CFP channel is also shown in
948 a separate panel.

949 **Movie S3. Time lapse movie showing two replicates of PlaCCI crossed to WIP4, PET111, or WOX5**
950 **during regeneration; Related to Figure 3.** Time stamp is shown in days:hours:minutes and represents time
951 post ablation. CYCB1;1-YFP is shown in yellow, CDT1a-CFP is shown in cyan and HTR13-mCherry is shown
952 in red. The CDT1a-CFP channel is also shown in a separate panel. In certain panels, other reporters are also
953 shown in yellow. In the top and bottom panels on the left, PET111 is shown in yellow. In the top right panel,
954 WOX5 is shown in yellow.

955 **Movie S4. Time lapse showing GSH burst following an ablation; Related to Figure 4.** Time stamp is
956 shown in days:hours:minutes. CYCB1;1-YFP is shown in yellow, CDT1a-CFP is shown in cyan, HTR13-
957 mCherry is shown in red, and blue CMAC is shown in grey. The blue CMAC channel is also shown in a
958 separate panel.

959

960

References

961

962

963

964

965

966

967

968

969

970

971

972

973

974

975

976

977

978

979

980

981

982

983

984

985

986

987

988

989

990

991

992

993

994

995

996

997

998

999

000

1. Hall, R.D., Riksen-Bruinsma, T., Weyens, G., Lefebvre, M., Dunwell, J.M., and Krens, F.A. (1996). Stomatal Guard Cells Are Totipotent. *Plant Physiol.* *112*, 889–892. [10.1104/pp.112.3.889](https://doi.org/10.1104/pp.112.3.889).
2. Sena, G., Wang, X., Liu, H.-Y., Hofhuis, H., and Birnbaum, K.D. (2009). Organ regeneration does not require a functional stem cell niche in plants. *Nature* *457*, 1150–1153. [10.1038/nature07597](https://doi.org/10.1038/nature07597).
3. Meyer, H.M., Teles, J., Formosa-Jordan, P., Refahi, Y., San-Bento, R., Ingram, G., Jönsson, H., Locke, J.C.W., and Roeder, A.H.K. (2017). Fluctuations of the transcription factor *atml1* generate the pattern of giant cells in the arabidopsis sepal. *Elife* *6*. [10.7554/eLife.19131.001](https://doi.org/10.7554/eLife.19131.001).
4. Winter, C.M., Szekely, P., Popov, V., Belcher, H., Carter, R., Jones, M., Fraser, S.E., Truong, T.V., and Benfey, P.N. (2024). SHR and SCR coordinate root patterning and growth early in the cell cycle. *Nature* *626*, 611–616. [10.1038/s41586-023-06971-z](https://doi.org/10.1038/s41586-023-06971-z).
5. Lee, L.R., and Bergmann, D.C. (2019). The plant stomatal lineage at a glance. *J. Cell Sci.* *132*, jcs228551. [10.1242/jcs.228551](https://doi.org/10.1242/jcs.228551).
6. Rahni, R., and Birnbaum, K.D. (2019). Week-long imaging of cell divisions in the Arabidopsis root meristem. *Plant Methods* *15*, 30. [10.1186/s13007-019-0417-9](https://doi.org/10.1186/s13007-019-0417-9).
7. Echevarria, C., Desvoyes, B., Marconi, M., Franco-Zorrilla, J.M., Lee, L., Umeda, M., Sablowski, R., Birnbaum, K.D., Wabnik, K., and Gutierrez, C. (2022). Stem cell regulators control a G1 duration gradient in the plant root meristem. *bioRxiv*, 2022.03.09.483577. [10.1101/2022.03.09.483577](https://doi.org/10.1101/2022.03.09.483577).
8. Han, S.-K., Herrmann, A., Yang, J., Iwasaki, R., Sakamoto, T., Desvoyes, B., Kimura, S., Gutierrez, C., Kim, E.-D., and Torii, K.U. (2022). Deceleration of the cell cycle underpins a switch from proliferative to terminal divisions in plant stomatal lineage. *Dev. Cell* *57*, 569–582.e6. [10.1016/j.devcel.2022.01.014](https://doi.org/10.1016/j.devcel.2022.01.014).
9. Sablowski, R., and Gutierrez, C. (2022). Cycling in a crowd: Coordination of plant cell division, growth, and cell fate. *Plant Cell* *34*, 193–208. [10.1093/plcell/koab222](https://doi.org/10.1093/plcell/koab222).
10. Desvoyes, B., and Gutierrez, C. (2020). Roles of plant retinoblastoma protein: cell cycle and beyond. *EMBO J.* *39*, e105802. [10.15252/embj.2020105802](https://doi.org/10.15252/embj.2020105802).
11. Gutierrez, C. (2016). 25 Years of Cell Cycle Research: What's Ahead? *Trends Plant Sci.* *21*, 823–833. [10.1016/j.tplants.2016.06.007](https://doi.org/10.1016/j.tplants.2016.06.007).
12. Sozzani, R., Cui, H., Moreno-Risueno, M.A., Busch, W., Van Norman, J.M., Vernoux, T., Brady, S.M., Dewitte, W., Murray, J.A.H., and Benfey, P.N. (2010). Spatiotemporal regulation of cell-cycle genes by SHORTROOT links patterning and growth. *Nature* *466*, 128–132. [10.1038/nature09143](https://doi.org/10.1038/nature09143).
13. Weimer, A.K., Matos, J.L., Sharma, N., Patell, F., Murray, J.A.H., Dewitte, W., and Bergmann, D.C. (2018). Lineage- and stage-specific expressed *CYCD7;1* coordinates the single symmetric division that creates stomatal guard cells. *Development* *145*, dev160671. [10.1242/dev.160671](https://doi.org/10.1242/dev.160671).
14. Han, S.-K., Qi, X., Sugihara, K., Dang, J.H., Endo, T.A., Miller, K.L., Kim, E.-D., Miura, T., and Torii, K.U. (2018). MUTE Directly Orchestrates Cell-State Switch and the Single Symmetric Division to Create Stomata. *Dev. Cell* *45*, 303–315.e5. [10.1016/J.DEVCEL.2018.04.010](https://doi.org/10.1016/J.DEVCEL.2018.04.010).
15. Menges, M., and Murray, J.A.H. (2002). Synchronous Arabidopsis suspension cultures for analysis of cell-cycle gene activity. *Plant J.* *30*, 203–212. [10.1046/j.1365-313x.2002.01274.x](https://doi.org/10.1046/j.1365-313x.2002.01274.x).
16. Menges, M., De Jager, S.M., Gruitsem, W., and Murray, J.A.H. (2005). Global analysis of the core cell cycle regulators of Arabidopsis identifies novel genes, reveals multiple and highly specific profiles of expression and provides a coherent model for plant cell cycle control. *Plant J.* *41*, 546–566.

- 001 10.1111/j.1365-313X.2004.02319.x.
- 002 17. Desvoyes, B., Noir, S., Masoud, K., López, M.I., Genschik, P., and Gutierrez, C. (2019). FBL17 targets
003 CDT1a for degradation in early S-phase to prevent Arabidopsis genome instability. *BioRxiv*.
004 10.1101/774109.
- 005 18. Desvoyes, B., Arana-Echarri, A., Barea, M.D., and Gutierrez, C. (2020). A comprehensive fluorescent
006 sensor for spatiotemporal cell cycle analysis in Arabidopsis. *Nature Plants*, 1–5. 10.1038/s41477-020-
007 00770-4.
- 008 19. Liu, L., Michowski, W., Kolodziejczyk, A., and Sicinski, P. (2019). The cell cycle in stem cell proliferation,
009 pluripotency and differentiation. *Nat. Cell Biol.* 21, 1060–1067. 10.1038/s41556-019-0384-4.
- 010 20. Hu, X., Eastman, A.E., and Guo, S. (2019). Cell cycle dynamics in the reprogramming of cellular identity.
011 *FEBS Lett.* 10.1002/1873-3468.13625.
- 012 21. Soufi, A., and Dalton, S. (2016). Cycling through developmental decisions: how cell cycle dynamics control
013 pluripotency, differentiation and reprogramming. 10.1242/dev.142075.
- 014 22. Zaveri, L., and Dhawan, J. (2018). Cycling to Meet Fate: Connecting Pluripotency to the Cell Cycle. *Front*
015 *Cell Dev Biol* 6, 57. 10.3389/fcell.2018.00057.
- 016 23. Gooh, K., Ueda, M., Aruga, K., Park, J., Arata, H., Higashiyama, T., and Kurihara, D. (2015). Live-cell
017 imaging and optical manipulation of Arabidopsis early embryogenesis. *Dev. Cell* 34, 242–251.
018 10.1016/j.devcel.2015.06.008.
- 019 24. Dubrovsky, J.G., Rost, T.L., Colón-Carmona, A., and Doerner, P. (2001). Early primordium
020 morphogenesis during lateral root initiation in Arabidopsis thaliana. *Planta* 214, 30–36.
021 10.1007/s004250100598.
- 022 25. Diehl, F.F., Sapp, K.M., and Vander Heiden, M.G. (2024). The bidirectional relationship between
023 metabolism and cell cycle control. *Trends Cell Biol.* 34, 136–149. 10.1016/j.tcb.2023.05.012.
- 024 26. Zhang, T., Noll, S.E., Peng, J.T., Klair, A., Tripka, A., Stutzman, N., Cheng, C., Zare, R.N., and Dickinson,
025 A.J. (2023). Chemical imaging reveals diverse functions of tricarboxylic acid metabolites in root growth
026 and development. *Nat. Commun.* 14, 2567. 10.1038/s41467-023-38150-z.
- 027 27. Tsukagoshi, H., Busch, W., and Benfey, P.N. (2010). Transcriptional regulation of ROS controls transition
028 from proliferation to differentiation in the root. *Cell* 143, 606–616. 10.1016/j.cell.2010.10.020.
- 029 28. Ribas, V., García-Ruiz, C., and Fernández-Checa, J.C. (2014). Glutathione and mitochondria. *Front.*
030 *Pharmacol.* 5, 151. 10.3389/fphar.2014.00151.
- 031 29. García-Giménez, J.L., Markovic, J., Dasí, F., Queval, G., Schnaubelt, D., Foyer, C.H., and Pallardó, F.V.
032 (2013). Nuclear glutathione. *Biochim. Biophys. Acta* 1830, 3304–3316. 10.1016/j.bbagen.2012.10.005.
- 033 30. Vernoux, T., Wilson, R.C., Seeley, K.A., Reichheld, J.P., Muroy, S., Brown, S., Maughan, S.C., Cobbett,
034 C.S., Van Montagu, M., Inzé, D., et al. (2000). The ROOT MERISTEMLESS1/CADMIUM SENSITIVE2
035 gene defines a glutathione-dependent pathway involved in initiation and maintenance of cell division
036 during postembryonic root development. *Plant Cell* 12, 97–110. 10.1105/tpc.12.1.97.
- 037 31. Koprivova, A., Mugford, S.T., and Kopriva, S. (2010). Arabidopsis root growth dependence on glutathione
038 is linked to auxin transport. *Plant Cell Rep.* 29, 1157–1167. 10.1007/s00299-010-0902-0.
- 039 32. Diaz Vivancos, P., Wolff, T., Markovic, J., Pallardó, F.V., and Foyer, C.H. (2010). A nuclear glutathione
040 cycle within the cell cycle. *Biochem. J* 431, 169–178. 10.1042/BJ20100409.
- 041 33. Vivancos, P.D., Dong, Y., Ziegler, K., Markovic, J., Pallardó, F.V., Pellny, T.K., Verrier, P.J., and Foyer,

- 042 C.H. (2010). Recruitment of glutathione into the nucleus during cell proliferation adjusts whole-cell redox
043 homeostasis in *Arabidopsis thaliana* and lowers the oxidative defense shield. *Plant J.* *64*, 825–838.
044 10.1111/j.1365-313X.2010.04371.x.
- 045 34. de Simone, A., Hubbard, R., de la Torre, N.V., Velappan, Y., Wilson, M., Considine, M.J., Soppe, W.J.J.,
046 and Foyer, C.H. (2017). Redox Changes During the Cell Cycle in the Embryonic Root Meristem of
047 *Arabidopsis thaliana*. *Antioxid. Redox Signal.* *27*, 1505–1519. 10.1089/ars.2016.6959.
- 048 35. Prasad, A., Sedlářová, M., Balukova, A., Rác, M., and Pospíšil, P. (2019). Reactive Oxygen Species as a
049 Response to Wounding: In Vivo Imaging in *Arabidopsis thaliana*. *Front. Plant Sci.* *10*, 1660.
050 10.3389/fpls.2019.01660.
- 051 36. Cools, T., Iantcheva, A., Maes, S., Van den Daele, H., and De Veylder, L. (2010). A replication stress-
052 induced synchronization method for *Arabidopsis thaliana* root meristems. *Plant J.* *64*, 705–714.
053 10.1111/j.1365-313X.2010.04361.x.
- 054 37. Hafemeister, C., and Satija, R. (2019). Normalization and variance stabilization of single-cell RNA-seq
055 data using regularized negative binomial regression. *Genome Biol.* *20*, 296. 10.1186/s13059-019-1874-1.
- 056 38. Ormerod, M.G., Tribukait, B., and Giaretti, W. (1998). Consensus report of the task force on
057 standardisation of DNA flow cytometry in clinical pathology. DNA Flow Cytometry Task Force of the
058 European Society for Analytical Cellular Pathology. *Anal. Cell. Pathol.* *17*, 103–110.
059 10.1155/1998/842306.
- 060 39. Hao, Y., Hao, S., Andersen-Nissen, E., Mauck, W.M., 3rd, Zheng, S., Butler, A., Lee, M.J., Wilk, A.J.,
061 Darby, C., Zager, M., et al. (2021). Integrated analysis of multimodal single-cell data. *Cell* *184*, 3573-
062 3587.e29. 10.1016/j.cell.2021.04.048.
- 063 40. Fragkos, M., Ganier, O., Coulombe, P., and Méchali, M. (2015). DNA replication origin activation in space
064 and time. *Nat. Rev. Mol. Cell Biol.* *16*, 360–374. 10.1038/nrm4002.
- 065 41. T, O., M, E., Mb, S., Pl, B., Okada, T., Endo, M., Singh, M.B., and Bhalla, P.L. (2005). Analysis of the
066 histone H3 gene family in *Arabidopsis* and identification of the male-gamete-specific variant AtMGH3.
067 *Plant J.* *44*, 557–568. 10.1111/j.1365-313X.2005.02554.x.
- 068 42. Rahni, R., Guillotin, B., Lee, L.R., and Birnbaum, K.D. (2024). A temporal map of division, chromatin
069 modification, and identity specification in the regenerating root. *bioRxiv*, 2024.01.09.574680.
070 10.1101/2024.01.09.574680.
- 071 43. Trapnell, C., Cacchiarelli, D., Grimsby, J., Pokharel, P., Li, S., Morse, M., Lennon, N.J., Livak, K.J.,
072 Mikkelsen, T.S., and Rinn, J.L. (2014). The dynamics and regulators of cell fate decisions are revealed by
073 pseudotemporal ordering of single cells. *Nat. Biotechnol.* *32*, 381–386. 10.1038/nbt.2859.
- 074 44. McInnes, L., Healy, J., and Melville, J. (2018). UMAP: Uniform Manifold Approximation and Projection for
075 Dimension Reduction. *arXiv [stat.ML]*.
- 076 45. Bizet, F., Hummel, I., and Bogeat-Triboulot, M.-B. (2015). Length and activity of the root apical meristem
077 revealed in vivo by infrared imaging. *J. Exp. Bot.* *66*, 1387–1395. 10.1093/jxb/eru488.
- 078 46. Velappan, Y., Signorelli, S., and Considine, M.J. (2017). Cell cycle arrest in plants: what distinguishes
079 quiescence, dormancy and differentiated G1? *Ann. Bot.* *120*, 495–509. 10.1093/aob/mcx082.
- 080 47. Rahni, R. (2020). Re: Generation of Identity and Stem Cell Activity in the *Arabidopsis* Root.
- 081 48. Nawy, T., Lee, J.-Y., Colinas, J., Wang, J.Y., Thongrod, S.C., Malamy, J.E., Birnbaum, K., and Benfey,
082 P.N. (2005). Transcriptional profile of the *Arabidopsis* root quiescent center. *Plant Cell* *17*, 1908–1925.
083 10.1105/tpc.105.031724.

- 084 49. Zhang, H., Zhang, T.T., Liu, H., Shi, D.Y., Wang, M., Bie, X.M., Li, X.G., and Zhang, X.S. (2018).
085 Thioredoxin-Mediated ROS Homeostasis Explains Natural Variation in Plant Regeneration. *Plant Physiol.*
086 176, 2231–2250. 10.1104/pp.17.00633.
- 087 50. Truernit, E., Bauby, H., Dubreucq, B., Grandjean, O., Runions, J., Barthélémy, J., and Palauqui, J.-C.
088 (2008). High-resolution whole-mount imaging of three-dimensional tissue organization and gene
089 expression enables the study of Phloem development and structure in Arabidopsis. *Plant Cell* 20, 1494–
090 1503. 10.1105/tpc.107.056069.
- 091 51. Plantin-Carrenard, E., Braut-Boucher, F., Bernard, M., Derappe, C., Foglietti, M.J., and Aubery, M. (2000).
092 Fluorogenic Probes Applied to the Study of Induced Oxidative Stress in the Human Leukemic HL60 Cell
093 Line. *J. Fluoresc.* 10, 167–167. 10.1023/A:1009499210857.
- 094 52. Toyota, M., Spencer, D., Sawai-Toyota, S., Jiaqi, W., Zhang, T., Koo, A.J., Howe, G.A., and Gilroy, S.
095 (2018). Glutamate triggers long-distance, calcium-based plant defense signaling. *Science* 361, 1112–
096 1115. 10.1126/science.aat7744.
- 097 53. Vatén, A., Dettmer, J., Wu, S., Stierhof, Y.-D., Miyashima, S., Yadav, S.R., Roberts, C.J., Campilho, A.,
098 Bulone, V., Lichtenberger, R., et al. (2011). Callose biosynthesis regulates symplastic trafficking during
099 root development. *Dev. Cell* 21, 1144–1155. 10.1016/j.devcel.2011.10.006.
- 100 54. Somssich, M., Khan, G.A., and Persson, S. (2016). Cell Wall Heterogeneity in Root Development of
101 Arabidopsis. *Front. Plant Sci.* 7, 1242. 10.3389/fpls.2016.01242.
- 102 55. Soni, N., and Bacete, L. (2023). The interplay between cell wall integrity and cell cycle progression in
103 plants. *Plant Mol. Biol.* 113, 367–382. 10.1007/s11103-023-01394-w.
- 104 56. Sablowski, R., and Carnier Dornelas, M. (2014). Interplay between cell growth and cell cycle in plants. *J.*
105 *Exp. Bot.* 65, 2703–2714. 10.1093/jxb/ert354.
- 106 57. Ruiz, S., Panopoulos, A.D., Herrerías, A., Bissig, K.-D., Lutz, M., Berggren, W.T., Verma, I.M., and Izpisua
107 Belmonte, J.C. (2011). A high proliferation rate is required for cell reprogramming and maintenance of
108 human embryonic stem cell identity. *Curr. Biol.* 21, 45–52. 10.1016/j.cub.2010.11.049.
- 109 58. Guo, S., Zi, X., Schulz, V.P., Cheng, J., Zhong, M., Koochaki, S.H.J., Megyola, C.M., Pan, X., Heydari, K.,
110 Weissman, S.M., et al. (2014). Nonstochastic reprogramming from a privileged somatic cell state. *Cell*
111 156, 649–662. 10.1016/j.cell.2014.01.020.
- 112 59. Pauklin, S., and Vallier, L. (2013). The cell-cycle state of stem cells determines cell fate propensity. *Cell*
113 155, 135–147. 10.1016/j.cell.2013.08.031.
- 114 60. Singh, A.M., Chappell, J., Trost, R., Lin, L., Wang, T., Tang, J., Wu, H., Zhao, S., Jin, P., and Dalton, S.
115 (2013). Cell-Cycle Control of Developmentally Regulated Transcription Factors Accounts for
116 Heterogeneity in Human Pluripotent Cells. *Stem Cell Reports* 1, 532–544.
117 10.1016/J.STEMCR.2013.10.009.
- 118 61. Dalton, S. (2015). Linking the Cell Cycle to Cell Fate Decisions. *Trends Cell Biol.* 25, 592–600.
119 10.1016/J.TCB.2015.07.007.
- 120 62. Jiang, D., and Berger, F. (2017). DNA replication–coupled histone modification maintains Polycomb gene
121 silencing in plants. *Science* 357, 1146–1149. 10.1126/science.aan4965.
- 122 63. Yang, H., Berry, S., Olsson, T.S.G., Hartley, M., Howard, M., and Dean, C. (2017). Distinct phases of
123 Polycomb silencing to hold epigenetic memory of cold in Arabidopsis. *Science* 357, 1142–1145.
124 10.1126/science.aan1121.
- 125 64. MacAlpine, D.M., and Almouzni, G. (2013). Chromatin and DNA replication. *Cold Spring Harb. Perspect.*

- 126 Biol. 5, a010207. 10.1101/cshperspect.a010207.
- 127 65. Hernández-Coronado, M., Dias Araujo, P.C., Ip, P.-L., Nunes, C.O., Rahni, R., Wudick, M.M., Lizzio, M.A.,
128 Feijó, J.A., and Birnbaum, K.D. (2022). Plant glutamate receptors mediate a bet-hedging strategy between
129 regeneration and defense. *Dev. Cell* 57, 451–465.e6. 10.1016/j.devcel.2022.01.013.
- 130 66. Züst, T., and Agrawal, A.A. (2017). Trade-Offs Between Plant Growth and Defense Against Insect
131 Herbivory: An Emerging Mechanistic Synthesis. *Annu. Rev. Plant Biol.* 68, 513–534. 10.1146/annurev-
132 arplant-042916-040856.
- 133 67. Guo, Q., Yoshida, Y., Major, I.T., Wang, K., Sugimoto, K., Kapali, G., Havko, N.E., Benning, C., and
134 Howe, G.A. (2018). JAZ repressors of metabolic defense promote growth and reproductive fitness in
135 *Arabidopsis*. *Proc. Natl. Acad. Sci. U. S. A.* 115, E10768–E10777. 10.1073/pnas.1811828115.
- 136 68. Huot, B., Yao, J., Montgomery, B.L., and He, S.Y. (2014). Growth-defense tradeoffs in plants: a balancing
137 act to optimize fitness. *Mol. Plant* 7, 1267–1287. 10.1093/mp/ssu049.
- 138 69. Burian, A., Barbier de Reuille, P., and Kuhlemeier, C. (2016). Patterns of Stem Cell Divisions Contribute to
139 Plant Longevity. *Curr. Biol.*, 1–10. 10.1016/j.cub.2016.03.067.
- 140 70. Savatin, D.V., Gramegna, G., Modesti, V., and Cervone, F. (2014). Wounding in the plant tissue: the
141 defense of a dangerous passage. *Front. Plant Sci.* 5, 470. 10.3389/fpls.2014.00470.
- 142 71. Lubkowitz, M. (2011). The oligopeptide transporters: a small gene family with a diverse group of
143 substrates and functions? *Mol. Plant* 4, 407–415. 10.1093/mp/ssr004.
- 144 72. Maughan, S.C., Pasternak, M., Cairns, N., Kiddle, G., Brach, T., Jarvis, R., Haas, F., Nieuwland, J., Lim,
145 B., Müller, C., et al. (2010). Plant homologs of the *Plasmodium falciparum* chloroquine-resistance
146 transporter, *PfCRT*, are required for glutathione homeostasis and stress responses. *Proc. Natl. Acad. Sci.*
147 *U. S. A.* 107, 2331–2336. 10.1073/pnas.0913689107.
- 148 73. Noctor, G., Queval, G., Mhamdi, A., Chaouch, S., and Foyer, C.H. (2011). Glutathione. *Arabidopsis Book*
149 9, e0142. 10.1199/tab.0142.
- 150 74. Voehringer, D.W., McConkey, D.J., McDonnell, T.J., Brisbay, S., and Meyn, R.E. (1998). Bcl-2 expression
151 causes redistribution of glutathione to the nucleus. *Proc. Natl. Acad. Sci. U. S. A.* 95, 2956–2960.
152 10.1073/pnas.95.6.2956.
- 153 75. Di Laurenzio, L., Wysocka-Diller, J., Malamy, J.E., Pysh, L., Helariutta, Y., Freshour, G., Hahn, M.G.,
154 Feldmann, K.A., and Benfey, P.N. (1996). The SCARECROW gene regulates an asymmetric cell division
155 that is essential for generating the radial organization of the *Arabidopsis* root. *Cell* 86, 423–433.
156 10.1016/s0092-8674(00)80115-4.
- 157 76. Helariutta, Y., Fukaki, H., Wysocka-Diller, J., Nakajima, K., Jung, J., Sena, G., Hauser, M.T., and Benfey,
158 P.N. (2000). The SHORT-ROOT gene controls radial patterning of the *Arabidopsis* root through radial
159 signaling. *Cell* 101, 555–567. 10.1016/s0092-8674(00)80865-x.
- 160 77. Sabatini, S., Heidstra, R., Wildwater, M., and Scheres, B. (2003). SCARECROW is involved in positioning
161 the stem cell niche in the *Arabidopsis* root meristem. *Genes Dev.* 17, 354–358. 10.1101/gad.252503.
- 162 78. Robbins, N.E., 2nd, Trontin, C., Duan, L., and Dinneny, J.R. (2014). Beyond the barrier: communication in
163 the root through the endodermis. *Plant Physiol.* 166, 551–559. 10.1104/pp.114.244871.
- 164 79. Michalopoulos, G.K., and DeFrances, M.C. (1997). Liver regeneration. *Science* 276, 60–66.
165 10.1126/science.276.5309.60.
- 166 80. Ookhtens, M., and Kaplowitz, N. (1998). Role of the liver in interorgan homeostasis of glutathione and
167 cyst(e)ine. *Semin. Liver Dis.* 18, 313–329. 10.1055/s-2007-1007167.

- 168 81. Huang, Z.Z., Chen, C., Zeng, Z., Yang, H., Oh, J., Chen, L., and Lu, S.C. (2001). Mechanism and
169 significance of increased glutathione level in human hepatocellular carcinoma and liver regeneration.
170 *FASEB J.* 15, 19–21. 10.1096/fj.00-0445fje.
- 171 82. Guillotin, B., Rahni, R., Passalacqua, M., Mohammed, M.A., Xu, X., Raju, S.K., Ramírez, C.O., Jackson,
172 D., Groen, S.C., Gillis, J., et al. (2023). A pan-grass transcriptome reveals patterns of cellular divergence
173 in crops. *Nature* 617, 785–791. 10.1038/s41586-023-06053-0.
- 174 83. Bargmann, B.O.R., and Birnbaum, K.D. (2010). Fluorescence Activated Cell Sorting of Plant Protoplasts.
175 *J. Vis. Exp.*, 2–5. 10.3791/1673.
- 176 84. Lee, L.R., Wengier, D.L., and Bergmann, D.C. (2019). Cell-type–specific transcriptome and histone
177 modification dynamics during cellular reprogramming in the *Arabidopsis* stomatal lineage. *Proceedings of*
178 *the National Academy of Sciences*, 201911400. 10.1073/pnas.1911400116.
- 179 85. Therneau, T.M. (2024). A Package for Survival Analysis in R.
- 180 86. Bewick, V., Cheek, L., and Ball, J. (2004). Statistics review 12: survival analysis. *Crit. Care* 8, 389–394.
181 10.1186/cc2955.
- 182 87. Huang, T., Guillotin, B., Rahni, R., Birnbaum, K., and Wagner, D. (2023). A rapid and sensitive multiplex,
183 whole mount RNA fluorescence in situ hybridization and immunohistochemistry protocol. *bioRxiv*,
184 2023.03.09.531900. 10.1101/2023.03.09.531900.